Inorganic Chemistry

Article

pubs.acs.org/IC

Can a Formally Zwitterionic Rhodium(I) Complex Emulate the Charge Density of a Cationic Rhodium(I) Complex? A Combined Synchrotron X-ray and Theoretical Charge-Density Study†

El-Eulmi Bendeif,[‡,§] Chérif F. Matta,*[,‡,⊥,¶] Mark Stradiotto,[¶] Pierre Fertey,[§] and Claude Lecomte*[,‡]

[‡]Laboratoire de Crystallographie, Résonance Magnétique et Modélisation CRM2, UMR CNRS 7036, Institut Jean Barriol, Faculté des Sciences et Technologies, Université de Lorraine, BP 70239, 54506 Vandoeuvre-les-Nancy, France

[§]Synchrotron Soleil, L'Orme des Merisiers Saint-Aubin, BP 48, 91192 Gif-sur-Yvette, France

[⊥]Department of Chemistry and Physics, Mount Saint Vincent University, Halifax Nova Scotia, Canada B3M 2J6

[¶]Department of Chemistry, Dalhousie University, Halifax, Nova Scotia, Canada B3H 4J3

Supporting Information

ABSTRACT: The molecular electron densities of structurally related cationic ([(κ^2-3-P^iPr$_2$-2-NMe$_2$-indene)Rh(COD)]-(CF_3SO_3), [**1c**](CF_3SO_3)) and formally zwitterionic ([(κ^2-3-P^iPr$_2$-2-NMe$_2$-indenide)Rh(COD)], **1z**) complexes were accurately determined using synchrotron bright-source X-ray radiation at 30 K followed by multipolar refinement (COD = η^4-1,5-cyclooctadiene). The densities were also obtained from density functional theory calculations with a large, locally dense basis set. A 28-electron ([Ar]3d^{10}) core of the Rh atom was modeled by an effective core potential to obtain a density that was then augmented with relativistic cores according to the Keith−Frisch approximation. Calculations were performed at the experimental geometry and after vacuum-phase geometry optimization starting from the experimental geometry. Experimental and calculated geometries and electron-density distributions show that the electron density and electronic structure in the region of the Rh center are not significantly altered by protonation of the aromatic ring and that formal removal of CF_3SO_3H from [**1c**](CF_3SO_3) affords a complex **1z** possessing substantial zwitterionic character (with a charge separation of ca. 0.9 electronic charge) featuring a negatively charged aromatic indenide framework. Further, the molecular electrostatic potentials of **1c** and **1z** exhibit similar topography around the metal, despite being drastically different in the vicinity of the indene or indenide portion of the cation (**1c**) and zwitterion (**1z**), respectively. Collectively, these observations obtained from high-level experimental and theoretical electron-density analysis confirm, for the first time, that appropriately designed zwitterionic complexes can effectively emulate the charge distribution found within ubiquitous cationic platinum-group metal catalyst complexes, in keeping with recent catalytic investigations.

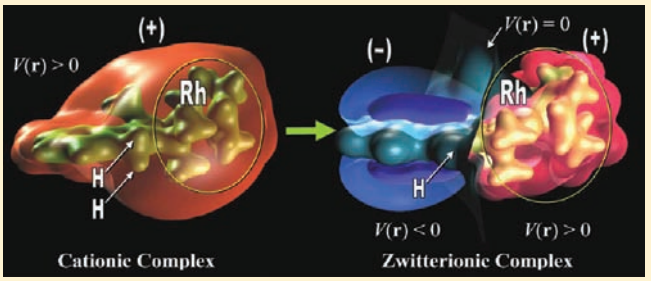

1. INTRODUCTION

Cationic platinum-group metal complexes (i.e., [L_nM]$^+X^-$) figure prominently in modern organometallic chemistry research, owing to the ability of such species to mediate challenging substrate transformations in a manner that in some cases cannot be achieved by the use of simple neutral complexes.[1−5] Although the study of cationic platinum-group metal complexes continues to enable breakthroughs in metal-mediated transformations, incompatibility with low- and high-polarity solvents can limit the effective operational scope of such salts.[3,6] Furthermore, the design of reactive cationic complexes is complicated by the fact that the outer-sphere counteranion (X^-) can influence profoundly the behavior of the complex via ion pairing, often in a manner that cannot be predicted easily.[7,8]

In an effort to combine the desirable reactivity properties of cationic species with the broad solvent tolerance of neutral complexes, the rational design of formally zwitterionic platinum-group metal complexes has garnered widespread attention within the field of organometallic chemistry.[9] While formal atom charges (e.g., on the basis of Lewis representations) do not represent true charges within a complex, it is plausible to envision that a zwitterionic motif that effectively emulates the charge distribution featured in a cationic complex might indeed be established if a formal charge separation between the ancillary ligand and coordinated cationic platinum-group metal fragment can be achieved. Several unique classes of formally zwitterionic platinum-group metal species that appear to meet such design criteria have emerged, owing to recent advances in ancillary ligand design.[9] Notably, comparative reactivity studies of structurally related cationic and zwitterionic platinum-group metal species reveal that the reactivity of such zwitterions is in many instances reminiscent of, and in some

Received: December 22, 2011
Published: March 2, 2012

   dx.doi.org/10.1021/ic2026347 | *Inorg. Chem.* 2012, 51, 3754−3769

cases superior to,[10−12] related cationic complexes.[9] Notwithstanding these recent synthetic and reactivity advances, no comprehensive experimental/computational analysis comparing the charge density within structurally analogous cationic and zwitterionic platinum-group metal complexes has appeared in the literature. Such investigations are critically needed in order to gain a better understanding of the electron distribution in conventional cationic platinum-group metal species, as well as to quantify the extent to which charge separation exists within a given zwitterionic framework.

Herein we report the first low-temperature [30(1) K] synchrotron crystallographic study of the electron density[13,14] combined with a theoretical analysis of the topology of the electron density within two structurally analogous cationic and zwitterionic platinum-group metal complexes. Analysis of the electron density is based on the quantum theory of atoms in molecules (QTAIM).[15−17]

Overarching goals of this study include (a) evaluating the extent to which commonly invoked organometallic bonding formalisms can represent experimentally observed/computationally predicted electron-density distributions and (b) assessing the capacity of a formally zwitterionic platinum-group metal complex to emulate the charge distribution featured within a structurally analogous cationic complex via formal charge separation. The cationic and zwitterionic complexes selected for this study are derived from 3-P^{i}Pr$_2$-2-NMe$_2$-indene (Chart 1); both the cation [(κ^2-3-P^{i}Pr$_2$-2-NMe$_2$-indene)Rh(COD)](CF$_3$SO$_3$) ([**1c**](CF$_3$SO$_3$)) and the zwitterionic species [(κ^2-3-P^{i}Pr$_2$-2-NMe$_2$-indenide)Rh(COD)] (**1z**) have proven useful in a range of catalytic applications involving σ-bond activation (COD = η^4-1,5-cyclooctadiene).[18,19] In contrast to conventional η^5-indenyl species,[20−25] platinum-group metal zwitterions such as **1z** can be viewed as comprising a formally cationic metal fragment [i.e., (COD)Rh$^+$ in **1z**] whose charge is counterbalanced by a sequestered, formally anionic, 10π-electron indenide unit that is incorporated into the backbone of the associated κ^2-P,N ligand. This paper demonstrates that this approach is, indeed, a viable one given the nearly identical charge distributions within the Rh coordination sphere of **1z** and **1c**.

Chart 1. Cationic (1c) and Formally Zwitterionic (1z) Rhodium(I) Complexes Featured in This Study

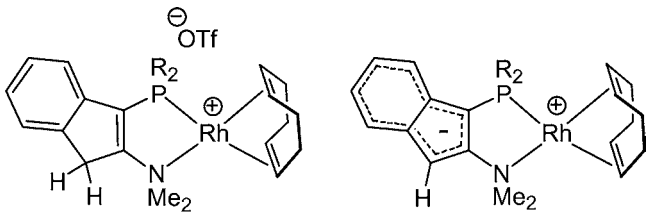

cationic
1cOTf, R = iPr
1c'OTf, R = Me

zwitterionic
1z, R = iPr
1z', R = Me

2. SYNCHROTRON X-RAY CRYSTALLOGRAPHIC EXPERIMENT

2.1. X-ray Diffraction Data Collection and Reduction. To investigate the charge-density distribution of the cationic and zwitterionic rhodium(I) species (**1c** and **1z**), accurate high-resolution single-crystal X-ray diffraction experiments at 30(1) K were performed at the CRISTAL beamline at Synchrotron Soleil (Saint Aubin, France). Good-quality single crystals of suitable size (typically 0.1 × 0.1 × 0.1 mm) were used for the data collection. They were fixed with silicon grease onto a short and thin microfabricated polyimide film attached to a solid nonmagnetic stainless steel pin (MicroMounts, MiTeGen) to avoid any unsteady motion due to the He flow and mounted on the goniometer head of the high-resolution Newport four-circle diffractometer equipped with an Oxford Atlas two-dimensional CCD detector (135 mm). To decrease thermal smearing effects, the samples were cooled from ambient temperature to 30(1) K over a period of 2 h using a Helium Cryoindustry cooling device. The temperature was calibrated beforehand using a K-type chromel−alumel thermocouple positioned at the same place on the crystal. The temperature stability was found to be within ±0.5 K during the duration of the measurements. It is worth noting that this is the first experiment at Synchrotron Soleil devoted to charge-density modeling.

In order to ensure high redundancies, the intensity data were accurately collected using ω oscillation scans of 1° frame^{-1} repeated at eight different φ positions at 2θ of 0°, 40°, and 70°. The low- and high-resolution reflections were measured with a radiation exposure time of 1 and 3 s, respectively. The shorter exposure times were used to accurately record the intense low-order data, avoiding pixel overflow or integration failure, while the high-angle sets utilized the longer exposure times to improve the measurement statistics. The sample-to-detector distance was 100 mm, and the wavelengths of the radiation used were 0.547 37 and 0.548 56 Å for **1z** and [**1c**](CF$_3$SO$_3$), respectively. These short wavelengths [close to the K edge of Rh (λ = 0.534 28 Å)] were chosen in order to minimize the absorption effects. Five different data sets were collected: a low-angle data set, using no attenuator, was collected first; then the same data collection was performed with an attenuator factor of 4; then very low-angle strong reflections were measured using an attenuator factor of 30; finally, two high-angle data sets were collected with and without an attenuator.

X-ray data were integrated using the *CrysAlisRed* program.[26] The absorption was small (due to the choice of the radiation wavelengths), but the data were, nevertheless, corrected by an empirical absorption correction. The different sets of measured reflections were subsequently merged and scaled using *SORTAV*.[27] A total of 1 355 281 and 812 400 reflection intensities collected up to the maximum resolution of sin θ_{max}/λ = 1.403 and 1.366 Å^{-1} were merged into 57 136 and 42 449 unique reflections for the cation ([**1c**](CF$_3$SO$_3$)) and zwitterion (**1z**), respectively. Data were 98% complete to sin θ/λ = 1.08 Å^{-1}, with all of the missing data above sin θ/λ = 0.96 Å^{-1}. The internal agreement factors for all data are $R_{int}(I)$ = 0.068 and 0.058 with average redundancies of 24 and 19 for [**1c**](CF$_3$SO$_3$) and **1z**, respectively.

2.2. Spherical Atom Refinement. The structures of the cationic and zwitterionic complexes [**1c**](CF$_3$SO$_3$) and **1z** (Figure 1) were solved using direct methods (*SHELXS97*)[28,29] and refined by full-matrix least squares on F^2 using the spherical atom model (*SHELXL97*),[28,29] with no constraints applied. All of the calculations were carried out using the *WinGX* package of crystallographic programs.[30,31] All of the non-H atoms were allowed anisotropic thermal motion. All H atoms were located in Fourier difference maps and refined initially with isotropic thermal displacement parameters. The full experimental details and refinement results for [**1c**](CF$_3$SO$_3$) and **1z** are summarized in Table 1.

dx.doi.org/10.1021/ic2026347 | Inorg. Chem. 2012, 51, 3754−3769

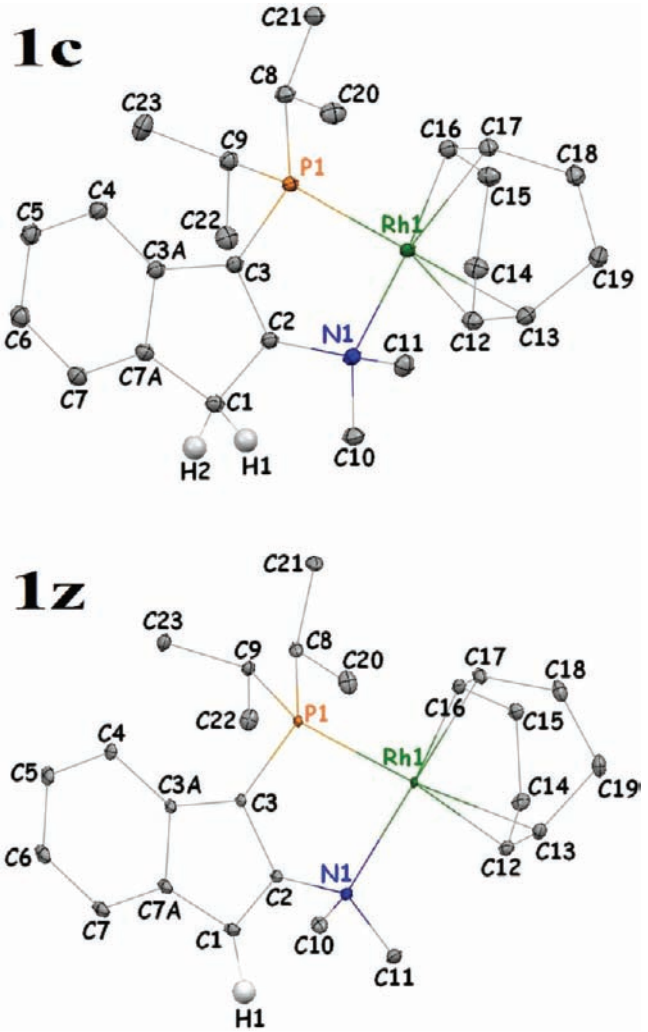

Figure 1. Experimental geometries of the cation **1c** (top) and the zwitterion **1z** (bottom), labeled with the atom numbering scheme. H atoms are removed for clarity (only H1 and H2 atoms are shown to distinguish **1c** from **1z**). The ORTEP 50% thermal ellipsoids are shown for all non-H atoms. Color scheme: Rh, dark green; P, orange; N, dark blue; C, dark gray; H, light gray.

2.3. Multipolar Refinement and Electronic Property Calculations. The multipole electron-density model of Hansen and Coppens,[32] as implemented in the program package *MoPro*,[33,34] was used. It allows for modeling of the valence electron density using atom-centered multipole functions (eqs 1 and 2):

$$\rho_{atom}(\mathbf{r}) = \rho_{core}(\mathbf{r}) + P_{val}\kappa^3\rho_{val}^{sph}(\kappa\mathbf{r}) + \rho_{multipolar}(\mathbf{r}) \quad (1)$$

where

$$\rho_{multipolar}(\mathbf{r}) = \sum_{l=0}^{l_{max}} \kappa'^3 R_l(\kappa'\mathbf{r}) \sum_{m=0}^{l} P_{lm\pm} Y_{lm\pm}(\theta, \phi) \quad (2)$$

As a starting point of the refinement, the independent atom model was used. The multipole refinement was undertaken using all positive unique reflections. Several models were tried, but the best results were obtained with a treatment that proceeded as follows. The multipole expansion was truncated at the hexadecapole level for all non-H atoms, while only bond-directed dipoles were applied for H atoms. The relativistic Dirac–Fock atomic wave functions[35,36] were used to describe both the core and valence-electron shells. The electronic configuration $5s^14d^8$ was used for Rh, with the $5s^1$ scattering contribution fixed as part of the core contribution. In the initial stages of refinement, constraints were applied to chemically

Table 1. Main Crystallographic Features, X-ray Diffraction Data Collection Parameters, and Final Results for 1c and 1z[a]

crystal data	cationic complex (**1c**)	zwitterionic complex (**1z**)
chemical formula	$(C_{25}H_{38}NPRh)^+\cdot(CF_3SO_3)^-$	$C_{25}H_{37}NPRh$
fw (g mol^{-1})	635.53	485.46
cell setting, space group	monoclinic, $P2_1/n$	monoclinic, $P2_1/c$
temperature (K)	30(1)	30(1)
a, b, c (Å)	9.9971(1), 20.1773(3), 14.1321(2)	9.6410(1), 16.8404(1), 14.3917(2)
β (deg)	103.452(1)	109.269(1)
V (Å^3)	2772.44(6)	2205.71(4)
Z	4	4
D_x (Mg m^{-3})	1.523	1.462
radiation type, wavelength (Å)	synchrotron, 0.54856	synchrotron, 0.54737
μ (mm^{-1})	0.335	0.458
crystal form, color	plate, orange	plate, brown
crystal size (mm)	0.130 × 0.120 × 0.100	0.125 × 0.125 × 0.100
diffractometer	Newport-Oxford	Newport-Oxford
data collection method	ω	ω
abs corrn	empirical (SORTAV)	empirical (SORTAV)
T_{min}, T_{max}	0.953, 0.988	0.934, 0.972
no. of measd, indep, and obsd reflns [$I > 2\sigma(I)$]	1355281, 57136, 47301	812400, 42449, 37162
R_{int}	0.068	0.058
θ_{min}, θ_{max} (deg)	1.56, 50.32	1.48, 48.38
sin θ_{max}/λ (Å^{-1})	1.403	1.366
	Spherical Refinements	
refinement on	F^2	F^2
R1 [$F^2 > 2\sigma(F^2)$], wR2(F^2), S	0.041, 0.119, 1.11	0.033, 0.094, 1.12
no. of reflns	47301	37162
no. of param	478	401
weighting scheme	calculated $w = 1/[\sigma^2(F_{obs}^2) + (0.0900P)^2 + 0.0052P]$ where $P = (F_{obs}^2 + 2F_{cal}^2)/3$	calculated $w = 1/[\sigma^2(F_{obs}^2) + (0.0612P)^2 + 0.0294P]$ where $P = (F_{obs}^2 + 2F_{cal}^2)/3$
$(\Delta/\sigma)_{max}$	0.01	0.004
$\Delta\rho_{max}$, $\Delta\rho_{min}$ (e Å^{-3})	2.676, −2.750	3.879, −2.299
	Multipole Refinements (MoPro Refinement Method)	
refinement on	F	F
R1 [$F > \sigma(F)$], wR2(F), S	0.029, 0.021, 1.97	0.026, 0.017, 1.73
no. data, restraints	57136, 84	42449, 80
no. of param	1791	1490
Ω weighting scheme	$w = 1/[\sigma^2(F_{obs}^2)]$	$w = 1/[\sigma^2(F_{obs}^2)]$
$\Delta\rho_{max}$, $\Delta\rho_{min}$ (e Å^{-3})	0.113, −0.120	0.227, −0.160

[a] $R1(F) = \sum[F_{obs} - k|F_{cal}|]/\sum F_{obs}$. $wR2(F) = [\sum w[F_{obs} - k|F_{cal}|]^2/\sum wF_{obs}^2]^{1/2}$. $S = [\sum w[F_{obs} - |F_{cal}|]^2/(n-p)]^{1/2}$. n is the number of reflections and restraints, and p is the total number of parameters refined.

dx.doi.org/10.1021/ic2026347 | Inorg. Chem. 2012, 51, 3754–3769

equivalent atoms. These were released progressively at the end of the refinement. The κ coefficients of H atoms were restrained to the value 1.160(1).[37] The κ' coefficients of the H atoms bound to C were restrained to the values reported previously,[38] namely, 1.18 with an allowed standard deviation of 0.001. The total number of electrons was kept constant to ensure electroneutrality of the complexes. The C−H bond lengths were restrained to their average neutron diffraction distances.[39] The anisotropic displacement parameters for the H atoms were estimated using the *SHADE2* web server[40] and fixed throughout the refinement.

The refinement resulted in featureless residual density maps (Figure S1 in the Supporting Information) and converged with final agreement factors of wR(F) = 2.10% and 1.70% for [**1c**](CF_3SO_3) and **1z**, respectively (Table 1), reflecting the better crystal quality for the **1z** complex. These low values demonstrate the high quality of the synchrotron data and refinement model. The Hirshfeld rigid-bond test[41] carried out after the multipole refinement was satisfactory. For all C−C bonds, the greatest difference between mean-squared displacement amplitudes never exceeds $\Delta Z^2 = 5(1) \times 10^{-4}$ Å^2, indicating an excellent deconvolution of thermal motion and electron density. As expected, the Rh1−C bonds had significantly higher mean-square displacement amplitudes along the bond directions [$\Delta Z^2 = 18(2)-30(3) \times 10^{-4}$ Å^2], exceeding the limit proposed by Hirshfeld (1×10^{-3} Å^2) for organic molecules. This is a consequence of the significant difference in atomic masses between the Rh and C atoms and of the nature of the metal-to-ligand bonding (Rh1−C═C). A successful rigid-bond test may be expected only for a metallocyclic system, as previously alluded to by Macchi et al.[42]

The topological analysis of the experimental electron density and bond critical point (BCP) localization and properties was performed using the *VMoPro*[34] and *MoProViewer*[34] programs. The experimental atomic properties (atomic volumes and charges) were obtained by numerical integration over the atomic basins using the program *WinxPRO 2009*.[43]

3. COMPUTATIONAL METHOD

3.1. Data Sets and Labeling Conventions. Six sets of data are analyzed and compared in this paper, three for each of **1c** and **1z**. Two sets of data are generated from the X-ray crystallographic experiment. The experimental sets of data for **1c** and **1z** are referred to as C-Xry and Z-Xry, respectively.

Four sets of data are obtained from quantum-chemical calculations, two for each of **1c** and **1z**. One set is obtained from a single-point calculation at the crystalline geometry, and the second set is obtained after a full (unconstrained) geometry optimization in the vacuum phase starting from the crystalline geometry. The first set will be labeled as sp (i.e., single point) and the second set as opt (i.e., fully optimized). These calculations in reference to **1c** (**1z**) are labeled C-sp (Z-sp) and C-opt (Z-opt), respectively.

3.2. General Approach and Electronic Structure Methods. All electronic structure calculations were performed on single isolated molecules (i.e., in vacuo) without the counterion (present in the crystal of [**1c**](CF_3SO_3)) or solvents. To balance the accuracy and cost of the calculations, the chosen electronic structure method is the density functional theory (DFT)[44,45] hybrid functional B3LYP[46,47] along with a *locally dense basis set* (LDBS),[48−51] being most dense at the Rh atom and its immediate surroundings, followed by a smaller (but still large) basis set for the intermediate surroundings, and finally by the smallest atomic basis set centered on atoms that are remote from the Rh1 atom (vide infra, section 3.3).

The calculation of an electron density that is both *accurate and continuous* in the region surrounding the Rh atom represents a challenge. First, the size of this system is relatively large (66 and 65 atoms for **1c** and **1z**, respectively, and 254 electrons counting all of the electrons of Rh). Given this size, a basis set is chosen to best represent the region surrounding the Rh atom, while minimizing the computational effort spent on the less relevant organic moieties that are distal to Rh in **1c** and **1z** (vide infra). A practical approximation to account, implicitly, for relativistic effects is the representation of the core electrons of the metal by an effective core potential (ECP; also termed pseudopotential, PP).[52−54] While a formally nonrelativistic Hamiltonian is employed, the ECP employed in this work, aug-cc-pVDZ-PP,[54] captures relativistic effects empirically, in addition to being correlation-consistent.[54,55] The second difficulty is associated with topological analysis of the electron densities obtained from calculations omitting core electrons due to the use of the ECP.[56] Such densities lack nuclear maxima at the nuclear positions of the heavy atoms treated by the ECP approximation. Consequently, the densities so obtained exhibit pathological topologies around the boundary(ies) of the core(s) replaced by the ECP.

These problems have been solved in an approximate manner by the recent pioneering work of Keith and Frisch.[57] Their approach essentially restores the missing electron density after the electronic structure calculation converges and the density (ρ_{ECP}), missing the core, is generated. This is achieved by augmenting ρ_{ECP} by the missing corresponding closed shells obtained from an all-electron scalar-relativistic density of the ground-state isolated atom.[57] Keith and Frisch calculated the atomic densities of all of the elements of the Periodic Table using the DFT/B3LYP hybrid functional[46,47] with the (large) universal Gaussian basis set[58] and with the incorporation of scalar-relativistic effects through the use of a Douglas−Kroll−Hess second-order Hamiltonian (DKH2).[59−62] The algorithm for augmenting the calculated ρ_{ECP} with missing cores has been implemented in the latest version of the *Gaussian* program,[63] which was used in all electronic structure calculations and geometry optimizations.

Upon geometry optimization convergence, the residual maximum force and residual root-mean-square forces on the nuclei of **1c** were 2.8×10^{-5} and 5×10^{-6} and those of **1z** were 3.1×10^{-5} and 5×10^{-6} hartree bohr^{-1} [atomic units (au)], respectively. Analysis in accordance with the QTAIM[15−17] was performed on the densities generated at the same level of theory of optimization and single-point calculations by use of the *AIMAll/AIMStudio* suite of programs.[64]

In total, 262 atomic integrations were performed. The average magnitude of the 262 atomic Lagrangians is 0.00014 ± 0.00018 au, with no single value exceeding 0.00109 au in magnitude.

3.3. Basis Set for Atoms Other Than Rh. As mentioned above (section 3.2), the electronic structure calculations were performed using a basis set that is densest at and in the immediate vicinity of the Rh atom. This LDBS approach has been shown to provide an excellent balance between the accuracy and practical feasibility of the calculation.[48−51]

Correlation-consistent-polarized atom-centered triple-ζ-quality basis set functions augmented with diffuse functions (aug-cc-pVTZ) are placed on all atoms (except P) that are formally bonded and/or in the immediate vicinity of the Rh atom ($d_{Rh-FAL} \leq 2.3$ Å). These atoms (N1, C12, C13, C16, and C17), along with the P atom, will be referred to as the *first atomic layer* (FAL). For the P atom, the basis set aug-cc-pV(T+d)Z, which includes tight d functions,[65] has been used and was obtained from the EMSL basis set exchange Web site.[66] The inclusion of tight d functions on second-row atoms is highly recommended for accurate work and is known to alter bond lengths and energetics significantly even at the Hartree−Fock level of theory.[65,67] Next, atoms that are directly bonded to any of the atoms of FAL will be labeled SAL (i.e., *second atomic layer*). The SAL atoms (C2, C3, C8, C9, C10, C11, C14, C15, C18, and C19) are described by a correlation-consistent-polarized atom-centered double-ζ-quality basis set function augmented with diffuse functions (aug-cc-pVDZ). Finally, all remaining atoms are described by the same basis set but without diffuse functions, i.e., by the cc-pVDZ atom-centered basis set.

3.4. Basis Set and ECP for the Rh Atom. The aug-cc-pVDZ-PP[54] ECP was used to replace 28 core electrons ([Ar]3d^{10}) of Rh. This core size has been recommended by Peterson et al. as because it

dx.doi.org/10.1021/ic2026347 | *Inorg. Chem.* 2012, 51, 3754−3769

has been shown to achieve a good spatial and energetic separability of the core and explicitly treated 17 valence electrons of Rh (electrons: $4s^2,4p^6,4d^8,5s^1$). This ECP has been optimized for Y–Pd 4d transition elements and has been shown to reproduce atomic valence spectra obtained from four-component all-electron multiconfiguration Dirac–Hartree–Fock calculations.[54]

4. RESULTS AND DISCUSSION

Figure 1 shows the crystal structure of the two studied complexes, the cationic complex $[(C_{25}H_{38}NPRh)]^+(CF_3SO_3)^-$ ($[\mathbf{1c}](CF_3SO_3)$) and the zwitterionic analogue ($C_{25}H_{37}NPRh$) (**1z**), along with the numbering scheme. Selected bond lengths and angles for both complexes are listed in Table S.1 in the Supporting Information, while Tables S.2 and S.3 in the Supporting Information list their experimental and optimized Cartesian coordinates.

4.1. Crystal Packing. A view of the crystal packing of the two complexes is displayed in Figure 2. The crystal structures of the two compounds are similar, and both form monoclinic crystals as described in Table 1.

*Salt of the Cationic Complex [**1c**](CF$_3$SO$_3$).* The crystal packing of $[\mathbf{1c}](CF_3SO_3)$ is built from chains of $(C_{25}H_{38}NPRh)^+$ cations running along the crystallographic *a* axis and alternating with the $(CF_3SO_3)^-$ anions (Figure 2). The cationic chains and anionic moieties are connected via anion–cation electrostatic forces and through eight C–H···O intermolecular interactions and two C–H···F weak contacts (C9—H9···F1 and C18—H181···F2; Table 2). Each $(C_{25}H_{38}NPRh)^+$ cation interacts with five $(CF_3SO_3)^-$ neighboring anions. All O atoms of the $(CF_3SO_3)^-$ anionic group are involved in hydrogen bonds: O2 acts as an acceptor four times and O1 three times, while O3 is an acceptor only once. There are no π–π interactions between the aromatic rings in the crystal packing. The molecular structure can be viewed as a donor–acceptor adduct, in which the $(CF_3SO_3)^-$ group plays an important role in the observed intermolecular interaction pattern.

*Zwitterionic Complex **1z**.* The molecular crystal packing of **1z** is composed of zigzag chains along the *c* axis (Figure 2) by the means of two categories of intermolecular interactions: two C–H···C interactions and three C–H···π system contacts (Table 2). Each molecule is surrounded by four symmetry-related molecules. The zigzag chains along the crystallographic *c* axis are linked through the weak C18—H182···C3A interaction between the cyclooctadiene group and aromatic rings. These zigzag chains are interconnected through another weak hydrogen bond C7–H7···C23 (Figure 2). As is clearly depicted in Figure 2, the nearly perpendicular orientation of the cyclic group explains the absence of π···π interactions between the aromatic rings in the crystal packing.

4.2. Molecular Geometries in the Vicinity of the Rh Atom. The Rh atom is tetracoordinated in both complexes, considering each olefin as a single ligand. On the basis of the bond path connectivity, however, the Rh atom can be considered as hexacoordinated because it is normally linked to an olefin ligand by *two*, rather than *one*, bond paths. The metal atom is bonded to the two alkene groups of the COD ligand (C*n*, *n* = 12, 13, 16, 17), as well as to P1 and N1 of a P,N-bidentate ligand (see Figure 1).

The four alkene C atoms of the COD ligand are not symmetrically linked to the Rh atom. Indeed, one can observe that, first, in both complexes the Rh1–C13 bond distance is approximately 0.04/0.05 Å (Xry/opt) shorter than the Rh1–C12 distance even though both are trans to the P1 atom. On the other hand, in **1c**, the Rh1–C16 bond is significantly longer compared to the Rh1–C17 bond [by 0.04/0.04 Å (Xry/opt)]; however, it is only slightly longer, by only 0.01/0.01 Å (Xry/opt), in **1z**. These differences in the Rh–C bond lengths are consistently reproduced in the optimized and experimental geometries and therefore can be reasonably attributed to the internal electronic structure of the molecules rather than to the crystal packing effects. Second, the Rh–C (COD) bond lengths trans to the P1 atom are significantly longer than those trans to the N1 atom in both **1c** and **1z**. These observations are in keeping with the greater trans influence of phosphorus over

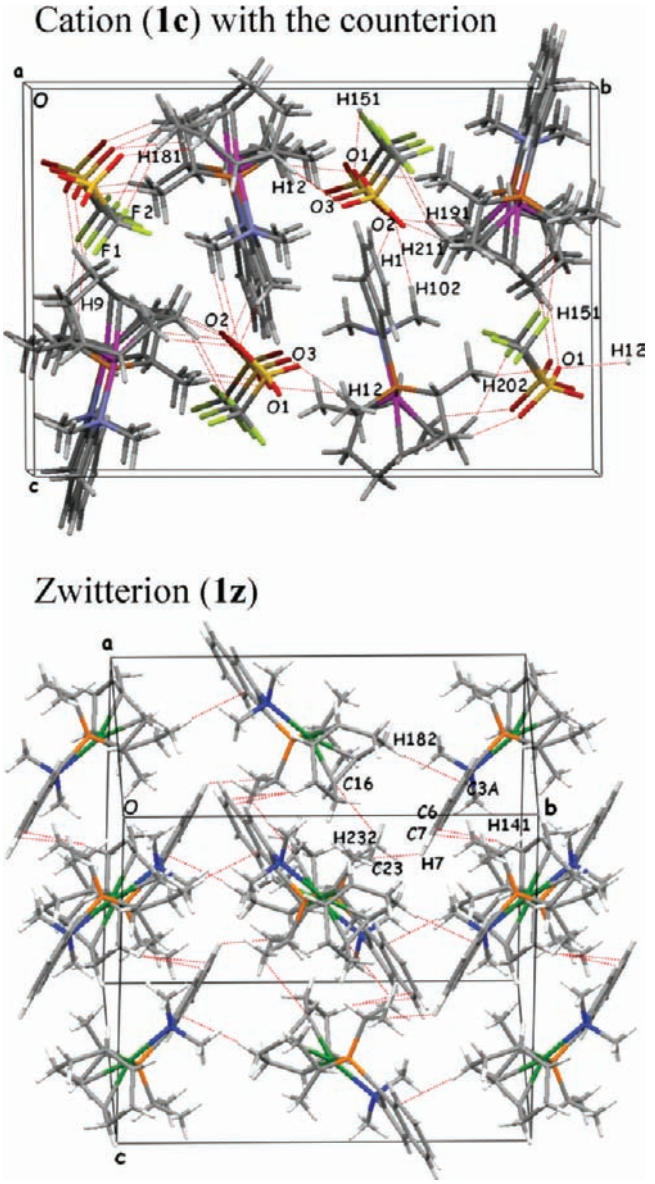

Figure 2. Representation of the crystal packing of the two complexes along with the corresponding unit cell. Note that the crystal of the cationic complex includes a counterion. Weak intermolecular interactions are indicated by red dotted lines. (The color scheme is the same as that in Figure 1, but in addition, the color scheme of the atoms in the counterion is as follows: O, red; F, light green; S, yellow.) (Top) Crystal packing of complex **1c** is viewed along the *a* axis showing the alternating $(C_{25}H_{38}NPRh)^+$ and $(CF_3SO_3)^-$ moieties. (Bottom) View along the *a* axis of the crystal packing of complex **1z**. The views were drawn using the program *Mercury*.[95]

dx.doi.org/10.1021/ic2026347 | *Inorg. Chem.* 2012, 51, 3754–3769

Table 2. Geometric Characteristics of Intra- and Intermolecular Hydrogen Bonds: Distances and Angles between the Donor and H and O Acceptor Atoms[a]

D−H···A	D−H (Å)	H···A (Å)	D···A (Å)	D−H···A (deg)
Cationic Complex **1c**				
C1−H1···O2	1.083(2)	2.322(2)	3.3811(3)	165(1)
C10−H102···O2	1.066(2)	2.507(1)	3.5637(6)	174(1)
C19−H191···O2	1.092(2)	2.606(14)	3.5060(1)	142(1)
C21−H211···O2	1.063(7)	2.389(11)	3.4113(6)	160(1)
C12−H12···O1	1.099(2)	2.607(12)	3.461(1)	134(1)
C15−H151···O1	1.092(2)	2.627(13)	3.649(1)	155(1)
C20−H201···O1	1.057(2)	2.534(13)	3.545(1)	164(1)
C12−H12···O3	1.099(2)	2.466(13)	3.4631(7)	146.6(9)
C9−H9···F1	1.099(2)	2.473(5)	3.509(1)	160(1)
C18−H181···F2	1.092(2)	2.556(8)	3.544(7)	150(1)
Zwitterionic Complex **1z**				
C7−H7···C23	1.083(3)	2.804(2)	3.5412(8)	125(3)
C23−H232···C16	1.059(3)	2.843(2)	3.4250(9)	123(3)
C−H···π Intermolecular Interactions[a]				
C18−H182···C3A	1.092(3)	2.587(1)	3.6449(8)	163(2)
C14−H141···C6	1.091(3)	2.723(2)	3.7853(7)	164(2)
C14−H141···C7	1.091(3)	2.754(3)	3.7761(7)	156(2)

[a]Interactions involving the F atoms in **1c** (H···F) are also listed. In the C18−H182···π interaction, the ring C atom closest to the H182 atom is C3A with a distance of 2.587(1) Å and an angle between C18, H182, and C3A of 163(2)°. The geometric characteristics of the C14−H141···π interactions show that the atoms that are closest to the H141 atom are C6 and C7 at respectively 2.723(2) and 2.754(3) Å. The atoms C14, H141, and C6 form an angle of 164(2)°, while the C14−H141−C7 angle is 156(2)°.

nitrogen and are similar to what has been found in other related rhodium complexes.[68]

The detailed examination of the square-planar arrangement around the Rh atom reveals two significant imperfections: First, the Rh1 atom is closer to the centers of the double bonds (C12═C13 and C16═C17) than to the N1 and P1 atoms, and the P1−Rh1−N1 bond angle deviates from 90°: Its value in **1c** is 86.5/83.4° (Xry/opt), and in **1z**, it is 85.8/83.2° (Xry/opt), and in both cases, it is likely attributable to the geometric requirements of the P,N-bidentate ligand. The deviations from 90° are thus quite similar in the two compounds and reasonably well-reproduced computationally.

As alluded to above, the distance between the midpoint (centroid) of the coordinated C12═C13 bonds (trans to P1) and the Rh1 atom is ∼0.1 Å longer than those between the Rh1 atom and the C16═C17 bonds (trans to N1), in keeping with the greater trans influence of phosphorus over nitrogen. Specifically, the Rh−alkene distance is longer by 0.09/0.11 Å (Xry/opt) in **1c** and 0.13/0.12 Å (Xry/opt) in **1z**. Further, the N1, P1, and Rh1 atoms and the centroids of the double bonds are not strictly coplanar. Whereas the double-bond centers do not deviate significantly [0.00/0.05 and 0.12/0.07 Å (Xry/opt)] from the mean plane defined by the Rh, P, and N atoms in **1z**, their deviations are more important in **1c** [0.56/0.50 and 0.37/0.40 Å (Xry/opt)]. Again, the close agreement between the experimental and optimized deviations from the plane suggests that these geometrical differences are characteristic of the molecules themselves rather than being a result of the crystal packing.

An important point to note in the above geometrical comparisons is that the agreement between the optimized and experimental geometry is slightly, but consistently, better for the zwitterionic compound (**1z**) than it is for the cationic compound (**1c**). This is probably because of the fact that while there are no counterions in the crystal of **1z**, the presence of the polar counterion in the crystal of **1c** is not addressed in the vacuum-phase optimization of the cationic portion of **1c** (carried out without the counterion).

Striking differences in the interatomic distances within the five-membered ring (5-MR) of the indene-derived fragment distinguish the cationic complex **1c** from its zwitterionic analogue **1z**. Thus, in the cationic form, the 5-MR ring exhibits bond-length alternation that characterizes nonaromatic rings; bonds C1−C7A [1.5109(5) Å], C1−C2 [1.5116(5) Å], and C3−C3A [1.4886(4) Å] are formally single bonds, whereas C2−C3 [1.3643(3) Å] and C3A−C7A [1.4161(5) Å] are formally double bonds. In the zwitterionic form **1z**, the indenide unit possesses a highly delocalized ring structure with the accompanying equalization of the bond lengths in the 5-MR, consistent with a Hückel aromatic $(4n + 2) = 10\pi$−electrons indenide anion (see Table S.1 in the Supporting Information for selected geometrical parameters).

4.3. Molecular Graphs. A molecular graph consists of a network of bond paths[69−71] defining the chemical structure in real three-dimensional space.[15−17] A bond path is found to link the nuclei of atoms considered bonded on the basis of chemical and spectroscopic evidence, with no counterexample(s) known to us. In other words, the molecular graph recovers the chemical structure. The presence or absence of a bond path is an all-or-none feature that does not distinguish, by itself, between the bonds of different order, strength, or mode.

Weak and borderline interactions are generally more ambiguously assigned on the basis of empirical evidence. In these cases, the bond path is a definitive indicator of chemical bonding when it exists; however, the absence of a bond path does not always negate an imminent bonding interaction. This is so because, in contrast to strong interactions, the presence or absence of a bond path of a weak bond can be highly sensitive to small electronic and/or geometrical changes. In these cases, an invaluable indicator of bonding is the delocalization index [DI or δ(A,B)],[72] also defined within QTAIM. This index is a continuously varying indicator of bonding that has been shown to be elevated between atoms sharing a bond path.[73,74] The DI constitutes a measure of the bond order that is exponentially correlated with the density at the BCP when a bond path exists.[75] An extensive description of the usage of DI in organometallic chemistry is given by Macchi and Sironi.[76]

The molecular graphs for the two complexes obtained from the theoretical densities after full energy minimization in the vacuum phase are displayed in Figure 3. (The molecular graphs obtained from the experimental densities and those calculated at the experimental geometries can also be found in Figure S2 in the Supporting Information.) The bond paths of strong interactions (arbitrarily defined as exhibiting values of $\rho_b \geq 0.05$ au) are displayed as solid gray lines linking the nuclei of the interacting atoms. Bond paths of weak interactions ($\rho_b < 0.05$ au) are plotted as pink solid lines in the experimental graphs and as dotted lines in the calculated graphs. The weak interactions found in these complexes are exclusively of the *hydrogen−hydrogen* (or H−H) bonding type where two closed-shell neutral (or similarly charged) H atoms share a bond path $H^{\delta\pm}\cdots H^{\delta\pm}$.[77−80] (The H−H bonding is distinct from the *dihydrogen* bonding $H^{\delta\mp}\cdots H^{\delta\pm}$, a hydrogen bond whereby the proton acceptor is a hydridic H atom.[81]) While the pattern of

dx.doi.org/10.1021/ic2026347 | Inorg. Chem. 2012, 51, 3754−3769

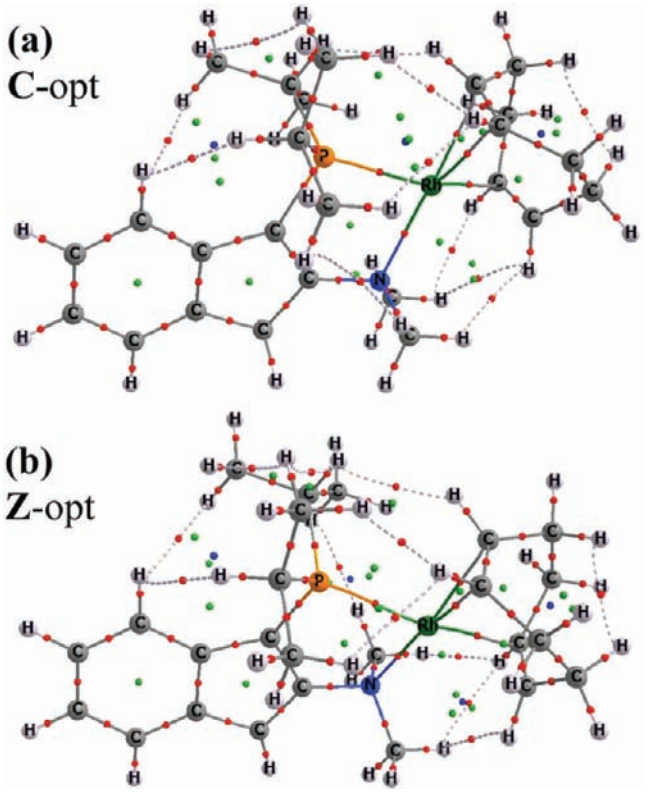

Figure 3. Representation of the molecular graphs of the two complexes obtained from the theoretically calculated electron density at the fully optimized geometry: (a) molecular graph of **1c** (without the counterion); (b) corresponding graphs of **1z**. The lines linking the nuclei are the bond paths. The bond paths corresponding to strong interactions ($\rho_b \geq 0.05$ au) are drawn as solid gray lines, while those corresponding to weak bonding interaction ($\rho_b < 0.05$ au) are depicted as dotted gray lines. The positions of atomic nuclei are indicated by small spheres following the same color scheme as that adopted in Figure 1. In addition, BCPs are indicated by small red spheres, RCPs by small green spheres, and cage critical points by small blue spheres. (The corresponding molecular graphs obtained from the experimental densities and from those theoretically calculated at the experimental geometries can be found in the Figure S2 in the Supporting Information.)

H−H bonding in these complexes is very interesting and contributes to their overall structural stability, a detailed discussion of such phenomena is beyond the scope of this manuscript and will be reported elsewhere.

The submolecular graphs that include only strong bonding interactions of the two complexes are similar, whether obtained from the X-ray density or calculated at the experimental or optimized geometries. The similarity is not only across the three molecular graphs of **1c** or **1z** but also between these two complexes (with the exception of the additional covalent C1−H2 bond present in the 5-MR of **1c**). A difference between the calculated and experimental molecular graphs is that, in all four theoretical densities, the bond path linking the nuclei of Rh1 and C13 is not observed, as is also the case in the experimental graph of **1z**. It is also noteworthy that the high ellipticity of the Rh1−C13 bond, which reflects the flatness of the density in this region, is such that a small perturbation in the charge density can lead to its disappearance and a "catastrophic" change of structure.[15] Similarly, unstable bond paths have already been observed in numerous transition-metal complexes.[82,83]

4.4. Bond Properties at Rhodium. The properties of the bonds surrounding Rh are collected in Table 3. In the following discussion and when quoting numerical values from Table 3, data will be quoted in the order Xry/sp/opt. All three sets of numerical entries are generally different, with the exception of bond lengths because their values from the Xry and sp sets are identical. Finally, there are no entries for the DI in the Xry data set because this quantity is only available from theoretical calculations, as it necessitates the atomic overlap matrix.

The three data sets entered in Table 3 exhibit a remarkable quantitative agreement (especially between Xry and sp values) not only among themselves for a given complex but also, and importantly, between the two different complexes. The similarity of the bonding descriptors of **1c** and **1z** is consistent with a largely unaltered catalytic Rh center in the zwitterion **1z**, which is, therefore, anticipated to have an activity similar to that of the parent compound, namely, the cationic complex **1c**. All listed bond properties, including those known to be particularly sensitive such as the Laplacian at the BCP, generally exhibit this relatively close similarity. Further, a given bond exhibits similar properties in both compounds, whether by comparing the experimental properties or both sets of calculated properties.

Bonds Involving the Rh Atom, Generalities. The experimental static deformation density map around the Rh metal center for **1z** is shown in Figure 4a (plane Rh1−P1−N1). A similar plot is found for the corresponding plane in **1c** (not shown). The typical 4d electron density for the Rh1 atom is clearly revealed by the aspherical density accumulation near the Rh1 atom directed toward the metal−ligand bisectors and by the charge depletion pointing toward the ligand. Figure 4b illustrates the map of the negative Laplacian function of the experimental density through the same plane (Rh1−P1−N1). As expected from ligand-field theory, the pronounced regions in which the valence density is locally depleted are observed along the Rh1−ligand directions, whereas the valence electron concentrations bisect the ligand directions.

We remark first that all six bonds involving the Rh atom are characterized by a relatively low electron density at the BCP (ρ_b), reaching a maximum of only ∼0.10−0.11 au in the case of bonding to the P and C atoms (Table 3). In all cases, bonds with Rh1 are all characterized with a positive Laplacian ($\nabla^2\rho_b$). This is a reflection of the minimal accumulation of density near the interatomic surfaces involving that atom, as can be gleaned from the small magnitudes of the negative curvatures (λ_1 and λ_2) compared to the magnitude of the positive curvature (λ_3).

The low magnitude of ρ_b and the positive $\nabla^2\rho_b$ are both characteristics of closed-shell interactions. On the other hand, all bonds involving Rh1 also exhibit a significant degree of electron sharing or "covalency". The electron-sharing (or delocalization) index [DI or δ(A,B)],[72] which provides a counting of the number of electron pairs shared between two given atomic basins A and B, shows that all of the bonds involving the Rh1 atom have a significant level of sharing, with δ(Rh1,X) falling in the range of 0.51−0.89 pairs. This degree of electron sharing is far greater than that of a closed-shell interaction, whereby the DI can fall to less than ∼0.1 pairs because there is no significant exchange between the two closed-shell atoms.

An independent measure of the covalency of a bond is the sign and magnitude of the total energy density at the BCP ($H_b = G_b + V_b$).[84] In covalent bonds, H_b is typically negative and of a nonnegligible magnitude. Table 3 shows that H_b values are negative for all interactions involving Rh1 but that their

dx.doi.org/10.1021/ic2026347 | Inorg. Chem. 2012, 51, 3754−3769

Table 3. Bond Properties within the Rhodium Coordination Sphere[a]

bond	system method[b]	BL[c]	BPL − BL[d]	δ(A,B)	ρ_b	$\nabla^2\rho_b$	λ_1	λ_2	λ_3	ε	V_b	G_b	H_b	G_b/ρ	H_b/ρ	$\lvert V_b\rvert/G_b$
Rh1−N1	C-Xry	2.2233(2)	0.0073		0.078	0.26	−0.09	−0.08	0.43	0.07	−0.10	0.08	−0.02	1.03	−0.26	1.25
	C-sp	2.2234	0.0016	0.508	0.075	0.27	−0.09	−0.06	0.42	0.38	−0.10	0.08	−0.02	1.11	−0.23	1.20
	C-opt	2.2699	0.0019	0.483	0.068	0.24	−0.08	−0.05	0.37	0.40	−0.09	0.07	−0.01	1.08	−0.20	1.19
	Z-Xry	2.2363(2)	0.0062		0.075	0.28	−0.10	−0.07	0.45	0.42	−0.10	0.09	−0.01	1.20	−0.13	1.11
	Z-sp	2.2363	0.0009	0.509	0.075	0.25	−0.09	−0.06	0.40	0.40	−0.10	0.08	−0.02	1.05	−0.23	1.22
	Z-opt	2.2719	0.0007	0.494	0.069	0.23	−0.08	−0.06	0.37	0.43	−0.09	0.07	−0.01	1.03	−0.21	1.20
Rh1−P1	C-Xry	2.3079(1)	0.0627		0.095	0.08	−0.11	−0.08	0.27	0.44	−0.12	0.07	−0.05	0.73	−0.52	1.71
	C-sp	2.3079	0.0035	0.886	0.103	0.12	−0.10	−0.08	0.30	0.14	−0.11	0.07	−0.04	0.68	−0.40	1.58
	C-opt	2.3365	0.0037	0.878	0.098	0.12	−0.09	−0.08	0.28	0.14	−0.10	0.07	−0.04	0.67	−0.38	1.56
	Z-Xry	2.3085(8)	0.0196		0.103	0.16	−0.11	−0.10	0.36	0.11	−0.14	0.09	−0.05	0.87	−0.48	1.56
	Z-sp	2.3085	0.0022	0.876	0.106	0.09	−0.10	−0.09	0.28	0.13	−0.11	0.07	−0.04	0.62	−0.41	1.66
	Z-opt	2.3702	0.0031	0.839	0.095	0.09	−0.09	−0.08	0.26	0.14	−0.09	0.06	−0.04	0.60	−0.37	1.61
Rh1−C12	C-Xry	2.2250(2)	0.0166		0.075	0.21	−0.08	−0.02	0.31	2.73	−0.09	0.07	−0.02	0.93	−0.27	1.29
	C-sp	2.2251	0.0404	0.545	0.082	0.17	−0.08	−0.04	0.30	0.87	−0.09	0.07	−0.02	0.80	−0.26	1.33
	C-opt	2.2535	0.0470	0.520	0.077	0.17	−0.07	−0.04	0.28	0.86	−0.08	0.06	−0.02	0.79	−0.25	1.31
	Z-Xry	2.2365(3)	0.2541		0.078	0.25	−0.08	−0.02	0.35	4.24	−0.10	0.08	−0.02	1.03	−0.26	1.25
	Z-sp	2.2365	0.0343	0.523	0.079	0.19	−0.07	−0.04	0.29	0.92	−0.09	0.07	−0.02	0.85	−0.26	1.30
	Z-opt	2.2450	0.0313	0.531	0.078	0.18	−0.07	−0.04	0.29	0.75	−0.08	0.06	−0.02	0.82	−0.25	1.31
Rh1−C13[e]	C-Xry	2.2673(2)	0.0027		0.073	0.20	−0.08	0.00	0.28	18.10	−0.09	0.07	−0.02	0.95	−0.27	1.29
	C-sp	2.2672		0.509												
	C-opt	2.3071		0.480												
	Z-Xry	2.2725(3)														
	Z-sp	2.2725		0.503												
	Z-opt	2.2921		0.503												
Rh1−C16	C-Xry	2.1717(2)	0.0280		0.096	0.21	−0.13	−0.03	0.37	2.86	−0.13	0.09	−0.04	0.93	−0.41	1.44
	C-sp	2.1717	0.0308	0.660	0.094	0.20	−0.09	−0.03	0.32	1.78	−0.11	0.08	−0.03	0.82	−0.30	1.37
	C-opt	2.1871	0.0431	0.651	0.091	0.20	−0.09	−0.03	0.31	2.52	−0.10	0.08	−0.03	0.84	−0.29	1.35
	Z-Xry	2.1193(2)	0.0345		0.097	0.26	−0.10	−0.00	0.37	23.80	−0.14	0.10	−0.04	1.03	−0.41	1.40
	Z-sp	2.1193	0.0133	0.710	0.104	0.19	−0.11	−0.07	0.37	0.65	−0.12	0.08	−0.03	0.79	−0.33	1.42
	Z-opt	2.1526	0.0198	0.687	0.097	0.19	−0.10	−0.05	0.34	0.87	−0.11	0.08	−0.03	0.79	−0.31	1.39
Rh1−C17	C-Xry	2.1347(2)	0.0352		0.098	0.25	−0.10	−0.05	0.40	0.92	−0.14	0.10	−0.04	1.02	−0.41	1.40
	C-sp	2.1347	0.0186	0.689	0.101	0.17	−0.11	−0.07	0.35	0.60	−0.11	0.07	−0.03	0.74	−0.32	1.43
	C-opt	2.1478	0.0227	0.679	0.098	0.17	−0.11	−0.06	0.34	0.65	−0.10	0.07	−0.03	0.74	−0.31	1.42
	Z-Xry	2.1272(3)	0.0482		0.099	0.22	−0.12	−0.04	0.38	1.99	−0.14	0.10	−0.04	1.01	−0.40	1.40
	Z-sp	2.1271	0.0153	0.697	0.102	0.19	−0.11	−0.06	0.36	0.77	−0.11	0.08	−0.03	0.79	−0.33	1.41
	Z-opt	2.1463	0.0175	0.685	0.098	0.18	−0.10	−0.06	0.35	0.74	−0.11	0.08	−0.03	0.78	−0.31	1.40
N1−C2	C-Xry	1.4624(2)	0.0061		0.263	−0.44	−0.61	−0.49	0.66	0.23	−0.58	0.24	−0.35	0.91	−1.33	2.42
	C-sp	1.4625	0.0004	0.962	0.264	−0.56	−0.52	−0.51	0.47	0.02	−0.35	0.10	−0.24	0.40	−0.93	3.33
	C-opt	1.4598	0.0004	0.963	0.265	−0.56	−0.52	−0.51	0.47	0.01	−0.35	0.11	−0.25	0.40	−0.93	3.33
	Z-Xry	1.4653(3)	0.0069		0.279	−0.69	−0.68	−0.57	0.56	0.21	−0.63	0.23	−0.40	0.82	−1.43	2.74
	Z-sp	1.4653	0.0001	0.925	0.256	−0.55	−0.50	−0.48	0.42	0.04	−0.37	0.11	−0.25	0.44	−0.99	3.22
	Z-opt	1.4727	0.0001	0.925	0.252	−0.53	−0.49	−0.47	0.42	0.04	−0.35	0.11	−0.24	0.43	−0.96	3.22
P1−C3	C-Xry	1.8117(2)	0.0097		0.177	−0.23	−0.25	−0.18	0.20	0.35	−0.30	0.12	−0.18	0.68	−1.02	2.50
	C-sp	1.8117	0.0012	0.760	0.166	−0.12	−0.23	−0.22	0.34	0.04	−0.29	0.13	−0.16	0.79	−0.97	2.23
	C-opt	1.8163	0.0010	0.774	0.166	−0.13	−0.23	−0.22	0.32	0.03	−0.29	0.13	−0.16	0.77	−0.97	2.26
	Z-Xry	1.7533(2)	0.0254		0.163	−0.10	−0.21	−0.15	0.26	0.45	−0.27	0.12	−0.15	0.73	−0.92	2.25
	Z-sp	1.7533	0.0008	0.837	0.182	−0.10	−0.26	−0.24	0.40	0.10	−0.34	0.16	−0.18	0.88	−1.01	2.15
	Z-opt	1.7522	0.0008	0.866	0.182	−0.10	−0.26	−0.24	0.40	0.11	−0.34	0.16	−0.18	0.88	−1.01	2.16
C12−C13	C-Xry	1.3911(3)	0.0512		0.312	−0.74	−0.66	−0.54	0.46	0.22	−0.76	0.29	−0.47	0.93	−1.51	2.62
	C-sp	1.3912	0.0019	1.393	0.319	−1.00	−0.71	−0.56	0.27	0.27	−0.48	0.11	−0.37	0.36	−1.15	4.19
	C-opt	1.3756	0.0018	1.416	0.330	−1.08	−0.74	−0.59	0.25	0.26	−0.51	0.12	−0.39	0.36	−1.18	4.25
	Z-Xry	1.3785(4)	0.0053		0.326	−0.77	−0.69	−0.53	0.45	0.31	−0.82	0.31	−0.51	0.95	−1.57	2.65
	Z-sp	1.3784	0.0016	1.412	0.327	−1.06	−0.73	−0.57	0.25	0.28	−0.50	0.12	−0.38	0.37	−1.18	4.20
	Z-opt	1.3772	0.0017	1.408	0.328	−1.07	−0.74	−0.58	0.25	0.27	−0.51	0.12	−0.39	0.37	−1.18	4.22
C16−C17	C-Xry	1.4129(3)	0.0100		0.293	−0.54	−0.56	−0.46	0.48	0.23	−0.70	0.28	−0.42	0.95	−1.43	2.50
	C-sp	1.4131	0.0025	1.283	0.306	−0.92	−0.67	−0.54	0.29	0.24	−0.44	0.11	−0.34	0.34	−1.09	4.19
	C-opt	1.3969	0.0025	1.294	0.316	−1.00	−0.70	−0.57	0.27	0.23	−0.47	0.11	−0.36	0.35	−1.13	4.26
	Z-Xry	1.4097(4)	0.0085		0.311	−0.70	−0.62	−0.52	0.44	0.21	−0.76	0.29	−0.47	0.93	−1.51	2.62
	Z-sp	1.4097	0.0026	1.265	0.307	−0.93	−0.67	−0.54	0.29	0.25	−0.45	0.11	−0.34	0.35	−1.10	4.17
	Z-opt	1.4002	0.0026	1.282	0.313	−0.97	−0.69	−0.56	0.28	0.25	−0.46	0.11	−0.35	0.35	−1.12	4.23
C2−C3	C-Xry	1.3643(3)	0.0050		0.309	−0.86	−0.72	−0.58	0.44	0.24	−0.74	0.26	−0.48	0.84	−1.56	2.85
	C-sp	1.3641	0.0005	1.604	0.325	−0.79	−0.68	−0.50	0.39	0.35	−0.45	0.13	−0.32	0.39	−0.99	3.57

dx.doi.org/10.1021/ic2026347 | Inorg. Chem. 2012, 51, 3754−3769

Table 3. continued

bond	system method[b]	BL[c]	BPL − BL[d]	δ(A,B)	ρ_b	$\nabla^2\rho_b$	λ_1	λ_2	λ_3	ε	V_b	G_b	H_b	G_b/ρ	H_b/ρ	$\lvert V_b\rvert/G_b$
	C-opt	1.3568	0.0006	1.612	0.329	−0.81	−0.69	−0.51	0.39	0.35	−0.46	0.13	−0.33	0.39	−1.00	3.58
	Z-Xry	1.4196(4)	0.0073		0.316	−0.83	−0.75	−0.54	0.46	0.38	−0.77	0.28	−0.49	0.88	−1.55	2.75
	Z-sp	1.4196	0.0013	1.259	0.291	−0.66	−0.58	−0.46	0.38	0.27	−0.36	0.10	−0.26	0.34	−0.90	3.69
	Z-opt	1.4289	0.0014	1.253	0.286	−0.64	−0.57	−0.45	0.38	0.27	−0.35	0.09	−0.25	0.33	−0.89	3.69

[a]All dimensioned quantities are in atomic units (au) except distances, which are in angstroms (Å). δ(A,B) is the DI between atoms A and B and is dimensionless. [b]C- refers to the cationic species (i.e., complex **1c**), and Z- refers to the zwitterionic species (i.e., complex **1z**). Xry refers to the experimental X-ray results. sp refers to the theoretical results obtained from a single-point calculation at the experimental geometry, and opt refers to the theoretical results obtained after a full geometry optimization starting from the experimental geometry. [c]BL = geometric bond length (internuclear distance). [d]BPL − BL = bond path length minus the geometric bond length (inter-nuclear distance). [e]This bond path is found only in the experimental density of **1c**.

magnitudes are generally small, reaching a maximum magnitude of only 0.05 au in the case of Rh1−P1 only. This criterion indicates some covalency, but that it is not pronounced, thereby confirming the conclusions drawn on the basis of ρ_b, $\nabla^2\rho_b$, and δ(Rh1,X).

Moreover, and according to the classification of Macchi et al.,[42] the nature of the Rh1−C*n* bonds clearly differs from that of purely ionic bonds (closed shell): First, the Rh1−C═C bond path topologies clearly show two independent endocyclic curved bond paths (Figure 5). This is in clear contrast to the purely closed-shell interactions that would have resulted in a T-shaped structure, as previously reported by Scherer and co-workers in their experimental electron-density analysis of scandium carbide complexes.[85] These inward curvatures are consistent with the classical Dewar−Chatt−Duncanson model,[86,87] as discussed earlier[42,88,89] and in another recent electron-density studies.[90] There has been some recent interest

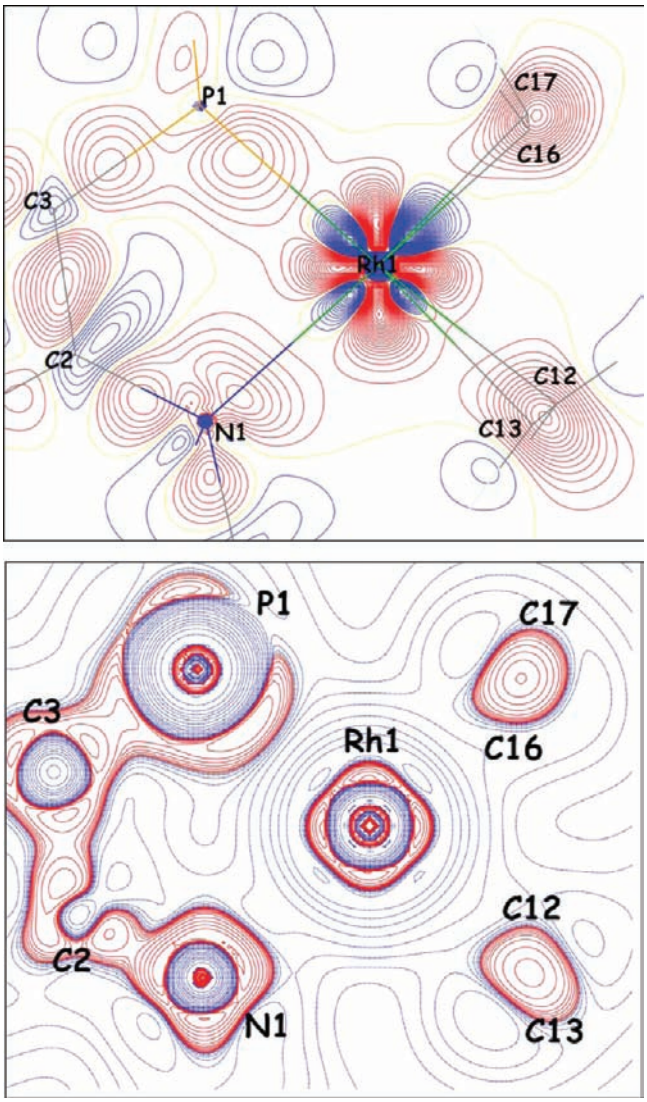

Figure 4. (a) Static experimental deformation density map for **1z** calculated in the plane Rh1−P1−N1. Contours are depicted at the 0.05 e Å^{-3} (ca. 0.007 au) level with positive contours as solid red lines, negative contours as solid blue lines, and the zero level as the faint yellow lines. (b) Negative Laplacian of the experimental electron density for **1z** in the same plane as part a. Positive contours are red lines, and negative contours are blue lines.

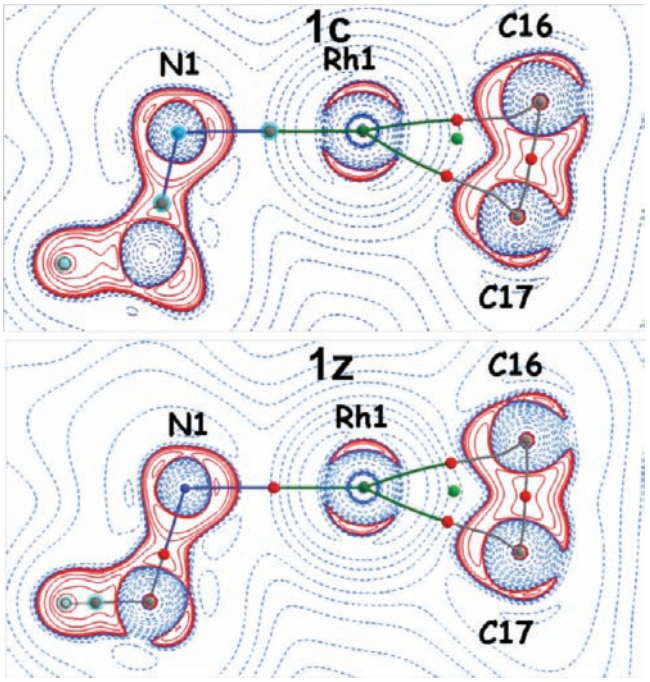

Figure 5. Maps of the Laplacian in the plane Rh1−C16−C17 obtained from the single-point "sp" calculation at the experimental geometry: (top) C-sp; (bottom) Z-sp. Positive contours are solid red lines, and negative contours are dashed blue lines. The lines linking the nuclear positions are the bond paths, and points surrounded by a diffuse blue halo are slightly out of the plane of the figure. Only those bond-path trajectories that lie on the plane of the figure are plotted, and those out of the plane are omitted. Red dots indicate the position of the BCPs and the green dots the location of the RCP.

dx.doi.org/10.1021/ic2026347 | *Inorg. Chem.* 2012, 51, 3754−3769

Table 4. Basic Atomic and Group Properties in 1c and 1z[a]

		cation (1c)				zwitterion (1z)			
atom or group	system method[b]	$q(\Omega)$	$N(\Omega)$	Vol(Ω)	$E(\Omega)$	$q(\Omega)$	$N(\Omega)$	Vol(Ω)	$E(\Omega)$
Rh1	Xry	0.290	44.710	125.1		0.295	44.705	125.3	
	sp	0.361	44.639	127.1		0.362	44.638	131.7	
	opt	0.353	44.647	132.5	−42.72191	0.369	44.631	136.7	−42.68391
				Atoms Bonded to Rh1					
P1	Xry	1.188	13.812	83.4		1.208	13.792	78.6	
	sp	1.664	13.336	72.0		1.802	13.198	67.2	
	opt	1.580	13.420	76.4	−358.76333	1.696	13.304	73.7	−358.67119
N1	Xry	−0.655	7.655	58.1		−0.810	7.810	57.1	
	sp	−0.900	7.900	58.3		−0.923	7.923	57.8	
	opt	−0.910	7.910	59.2	−57.77100	−0.916	7.916	58.8	−57.76794
C12	Xry	−0.158	6.158	65.2		−0.157	6.157	63.1	
	sp	−0.106	6.106	63.2		−0.121	6.121	65.9	
	opt	−0.102	6.102	62.9	−39.99436	−0.115	6.115	65.9	−39.98371
C13	Xry	−0.103	6.103	59.1		−0.224	6.224	59.8	
	sp	−0.130	6.130	66.5		−0.116	6.116	63.9	
	opt	−0.118	6.118	65.8	−39.98435	−0.108	6.108	63.2	−39.99167
C16	Xry	−0.380	6.380	68.6		−0.222	6.222	63.5	
	sp	−0.116	6.116	64.0		−0.108	6.108	62.2	
	opt	−0.103	6.103	63.0	−39.96546	−0.102	6.102	62.9	−39.96419
C17	Xry	−0.239	6.239	68.2		−0.336	6.336	67.8	
	sp	−0.102	6.102	62.2		−0.110	6.110	60.5	
	opt	−0.095	6.095	61.6	−39.98477	−0.100	6.100	61.1	−39.98305
				Groups[c]					
indene/indenide	Xry	0.170	59.830	957.8		−0.754	59.752	943.5	
	sp	−0.197	60.197	952.9		−0.924	59.924	960.1	
	opt	−0.185	60.185	956.2	−363.54921	−0.918	59.918	968.9	−363.09463
COD	Xry	−1.324	61.324	1113.8		−0.410	60.409	1026.8	
	sp	0.071	59.929	1040.8		−0.062	60.062	1039.2	
	opt	0.092	59.908	1042.6	−327.26702	−0.052	60.052	1048.6	−327.31458
R_N (=NMe_2)	Xry	0.286	24.714	483.8		−0.105	25.104	490.8	
	sp	−0.167	25.167	443.5		−0.255	25.255	445.9	
	opt	−0.176	25.176	455.8	−141.10724	−0.252	25.252	457.7	−141.14259
R_P (=P*i*Pr_2)	Xry	1.800	63.200	1154.5		0.997	64.004	1123.6	
	sp	0.931	64.069	1092.4		0.881	64.119	1083.1	
	opt	0.916	64.084	1124.9	−607.25375	0.855	64.145	1128.2	−607.22854
				SUM[d]					
	Xry	1.190	253.810	3843.8		0.023	253.974	3710.0	
	sp	0.999	254.001	3656.7		0.002	253.998	3659.9	
	opt	1.000	254.000	3712.0	−1481.89913	0.003	253.997	3740.1	−1481.46426
counterion	Xry	−0.702	73.702	832.3					
cation + counterion	Xry	0.488	327.512	4676.1					

[a]All dimensioned quantities are in atomic units (au). [b]Xry = experimental X-ray results, sp = theoretical results obtained from a single-point calculation at the experimental geometry, and opt = results from theory after geometry optimization. [c]The groups include the following atoms: indene (in **1c**)/indenide (in **1z**) = [C1, C2, C3, C3A, C4, C5, C6, C7, C7A, H1, H2 (in **1c** only), H4, H5, H6, H7], COD = (C12, C13, C14, C15, C16, C17, C18, C19, H12, H13, H141, H142, H151, H152, H16, H17, H181, H182, H191, H192), R_N = (N1, C10, C11, H101, H102, H103, H111, H112, H113), and R_P = (P1, C20, C21, C9, C22, C23, H8, H201, H202, H203, H211, H212, H213, H9, H221, H222, H223, H231, H232, H233). [d]The sum over the experimental atomic properties in the case of **1c** is that on all of the atoms of the cationic species without the counterion.

in this type of bent bond paths occurring, for example, in the case of bonding between Co and a C═C double bond.[91]

On the other hand, the bond paths for Rh1−C*n* interactions are longer than the interatomic distances (see Table 3), reflecting that these interactions are not those of an ideal metallacycle characterized by a straight M−C bond path. Thus, not all of the bonds involving the Rh1 atom can be simply classified into one category because they have some of the characteristics of both closed-shell and covalent bonding. We now discuss each bonding interaction occurring in the vicinity of the metal center.

Rh1−N1 Bond. This bond is slightly longer in **1z** compared to **1c** in the optimized geometries (by 0.002 Å) and had the same tendency in the experimental data with a difference of 0.013 Å. The optimized bond length is longer than the experimental one by 0.047 and 0.036 Å for **1c** and **1z**, respectively. The electron density at the BCP, ρ_b, in the case of **1c** is 0.078/0.075/0.068 and is 0.075/0.075/0.069 for the **1z** complex, indicating a very similar bond order/strength. The electron density at the Rh1−N1 BCP is relatively low ($\rho_b \approx$ 0.07−0.08 au) compared to a (polar) covalent bond such as N1−C2 ($\rho_b \approx$ 0.25−0.28 au), as may be expected (Table 3).

dx.doi.org/10.1021/ic2026347 | *Inorg. Chem.* 2012, 51, 3754−3769

The sharing index in both complexes indicates a very similar sharing of ∼0.5 pairs between Rh1 and N1.

Rh1−P1 Bond. Experimentally, this bond is of equal length in both **1c** and **1z** within experimental uncertainties. In the optimized geometries, however, this bond in **1z** is slightly longer than its counterpart in **1c** by 0.034 Å. Further, the optimized bond length is longer than the experimental one by 0.029 and 0.062 Å for **1c** and **1z**, respectively. For **1c**, ρ_b has the values 0.095/0.103/0.098, which are close to those in **1z** (0.103/1.06/0.095). These values of the electron density at the Rh1−P1 BCP are slightly higher than any of the other Rh−X bonds in the two complexes (Table 3). The particularly good agreement between all of the Rh1−P1 bond properties obtained from the experiment and the single-point calculation adds further support to the quality of the basis set and the underlying level of theory including the recommended addition of a set of tight d functions.[65]

Rh1−Cn (n = 12, 13, 16, 17) Bonds. The bond paths associated with these interactions are all observed in the six data sets, with the exception of the Rh1−C13 bond path, which is only observed in the experimental density of the **1c** complex. The elevated ellipticity of the Rh1−C13 bond path, ε = 18.10, is indicative of a topologically unstable interaction (vide supra). In the calculated densities, this BCP has coalesced with the ring critical point (RCP), annihilating the corresponding (unstable) bond path. It is unsurprising that they are neither observed in any of the four calculated densities nor in the experimental density of **1z**. Once again, experiment and theory yield a consistent picture.

Comparing the two arms of the Rh1−C12−C13 triangle, the Rh1−C12 distance is shorter in both compounds and in both of the calculated and experimental geometries than the Rh1−C13 distance. The differences ($d_{RH1-C12} - d_{RH1-C13}$, in Å) are −0.042 (C-Xry/sp), −0.054 (C-opt), −0.036 (Z-Xry/sp), and −0.047 (Z-opt). In the optimized geometry of **1c**, Rh1−C13 is also longer than Rh1−C12 by 0.0536 Å, with this difference being very similar to that found in the optimized geometries of **1z** (0.0471 Å). These geometrical comparisons indicate that the two interactions are very similar in the two complexes. The lack of the Rh1−C13 bond path represents an exemplary case, whereby the DI is invaluable in quantifying an incipient bonding interaction.

The strength of the Rh1−C13 interaction, as measured by the DI, shows very little discrepancy for both **1c** and **1z** relative to the DI for Rh1−C12 in both complexes. The values of the DI in both compounds and both bonds, whether from the sp or opt calculations, compare very well. Thus, to two decimals, we have [**1c**]/[**1z**], δ(Rh1,C12) = [0.55/0.52]/[0.52/0.53], and δ(Rh1,C13) = [0.51/0.48]/[0.50/0.50]. The corresponding differences [δ(Rh1,C12) − δ(Rh1,C13)] are 0.04 (C-sp), 0.04 (C-opt), 0.02 (Z-sp), and 0.03 (Z-opt). The magnitudes of these differences indicate an insignificant variation in the extent of electron delocalization between the Rh1 and both C atoms, which can be taken as 0.5 pairs. The two bonds, Rh1−C12 and Rh1−C13, can, thus, be expected to be of comparable strength in both complexes.

All descriptors of bonding indicate that the Rh1−C16/Rh1−C17 bonding interactions (ρ_b ranging from 0.091 to 0.104 au; trans to N) are significantly stronger than those of the Rh1−C12/Rh1−C13 pair (ρ_b ranging from 0.073 to 0.082 au; trans to P) in both complexes. The ρ_b values listed in Table 3 indicate that the two bonds (Rh1−C16 and Rh1−C17) have very similar values in all data sets, with a modestly stronger Rh1−C17 interaction in both complexes. Even this subtle difference appears to be reproduced quite faithfully in the two complexes **1c** and **1z**. The sharing index ranges from 0.65 to 0.71, and therefore both bonds in the two complexes engender a delocalization of ∼0.7 pairs between the Rh and C atoms.

Remaining Bonds around Rh1. There is nothing unusual in the topological properties of the remaining bonds: N1−C2, P1−C3, C12−C13, C16−C17, and C2−C3. All of these bonds in both compounds and in all data sets exhibit, without exception, a negative Laplacian at the BCP, a negative total energy density H_b with a magnitude and order higher than the bonds involving the Rh1 atom, high values of ρ_b, and an elevated δ(A,B). The properties of these bonds listed in Table 3 also indicate that experiment and theory are in good agreement and that the bond properties in the zwitterionic complex **1z** are very similar to their counterparts in the cationic complex **1c**.

4.5. Properties of the Atoms Proximal to Rh. Table 4 provides a listing of some basic QTAIM topological properties for both complexes: atomic charges $q(\Omega)$, atomic electron populations $N(\Omega)$, atomic volumes Vol(Ω), and atomic energies $E(\Omega)$. The values of $q(\Omega)$, $N(\Omega)$, and Vol(Ω) are for the three data sets. The listing of $E(\Omega)$ in the table is exclusively for the "opt" data set because only in this case are the virial-based atomic energies defined without the necessity of a heuristic partitioning of the term arising from virial of nonvanishing forces on the nuclei. The table lists the individual atomic properties of Rh and its immediate surrounding atoms only, namely, the six atoms sharing a bond path with Rh. The properties of the remaining atoms are included in the sum of the group to which they belong (Table 4 and Figure 6). Figure 6 depicts the summed atomic properties on five chosen groups that represent the different regions surrounding Rh. The groups include P*i*Pr$_2$, COD, NMe$_2$, the indene/indenide moiety, and the Rh center itself.

Precision of the Numerical Atomic Integrations. As can be seen at the bottom of Table 4, the sum of all of the atomic charges for **1z** is 0.023/0.002/0.003 au for the three data sets. For a system with 254 electrons, this constitutes a numerical integration error of 0.01/0.00/0.00%, respectively. In the case of **1c**, the sum of atomic charges is 0.999 and 1.000 au for the sp and opt data sets, with an error of 0.00% in both cases. In the crystal, each molecule of **1c** (254 electrons) is accompanied by counterion molecule $CF_3SO_3^-$ bearing 74 electrons. The number of electrons in the neutral salt (i.e., [**1c**](CF_3SO_3)) is, thus, 328 electrons. The sum of all charges for a neutral pair (**1c** featuring its counterion) is 0.488 au instead, which yields a global relative error of 0.15% (0.488/328), higher than that in the case of Z-Xry but still acceptable and in line with other experimental results. This error is probably due to the more diffuse density in the inter-ion regions and larger integration volume of the cation−anion pair compared to the more compact single-component molecular species in the case of the zwitterions **1z**. The quoted experimental atomic electron populations $N(\Omega)$ that are listed in Table 4, thus, can be considered as having an uncertainty of ∼0.2% of their quoted value because of this integration error.

The Rh1 Atom. All three data sets for both the cation **1c** and zwitterion **1z** indicate a net charge on Rh of ca. +0.3−0.4 au. The net charge on this atom is very slightly higher (in the second decimal) in **1z**, in keeping with the conceptual view that the design of the zwitterionic complex **1z** succeeds in emulating the characteristics of the cationic species **1c** with respect to the net charge at Rh. In all cases, q_{opt}(Rh1) > q_{sp}(Rh1) > q_{Xry}(Rh1),

dx.doi.org/10.1021/ic2026347 | *Inorg. Chem.* 2012, 51, 3754−3769

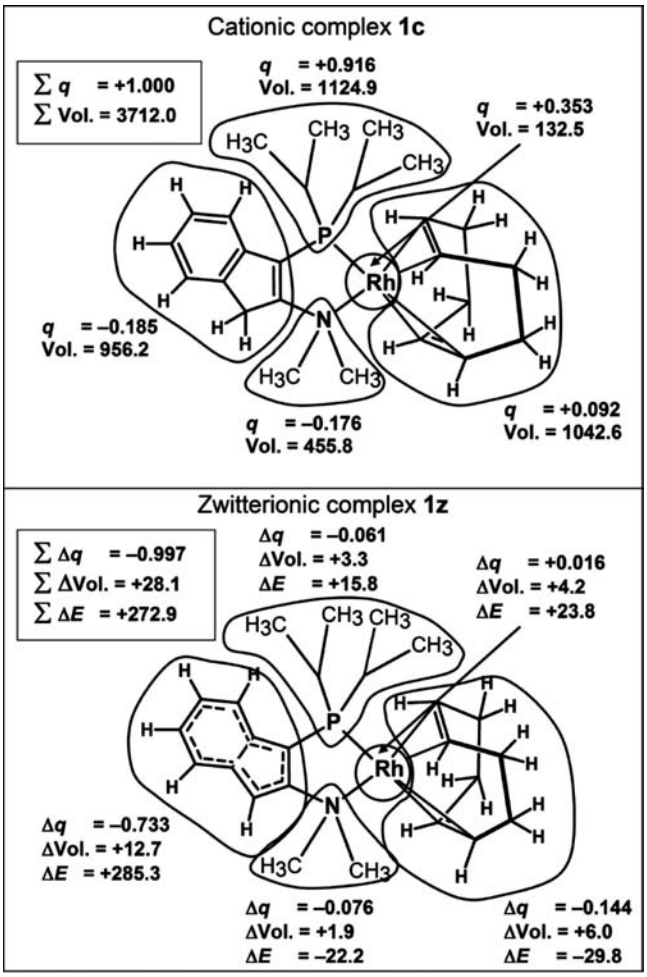

Figure 6. Group properties (P) of complexes **1c** (top) and their changes [$\Delta P = P(\mathbf{1z}) - P(\mathbf{1c})$] in **1z** (bottom) calculated from the densities obtained after full geometry optimizations (Opt). Charges (q) and volumes (Vol) are given in au and energies (E) in kcal mol^{-1} shown.

where the magnitude of the difference $|q_{opt}(\mathrm{Rh1}) - q_{Xry}(\mathrm{Rh1})|$ equals 0.063 au in **1c** and 0.074 au in **1z**. These results are consistent with a set of lower-level calculations (optimization and densities obtained at the DFT-B3LYP/6-31G(d,p) level with the LANL2DZ ECP replacing a 28 electrons core of Rh) carried out on truncated models (level 2, **1c′** and **1z′**; Chart 1), whereby the charge on Rh1 was found to be +0.33 au in **1c′** and +0.36 au in **1z′**; for comparison, at the higher level (level 1), q(Rh1) ≈ +0.35 au **1c** and ≈ +0.37 au in **1z**.

The volume of the Rh1 atom is consistently slightly larger in **1z** than in **1c** (by 0.2/4.6/4.2 au) despite the atom's slightly lower electron population in the former complex. The lower energy of Rh1 in **1c** indicates a higher stability (by 24 kcal mol^{-1}) of the outer-shell electrons (treated explicitly) compared to **1z**. A more stable Rh1 in **1c** is consistent with its slightly higher electron population than in **1z**. However, these observations regarding the stability of the Rh1 atom do not take into account core polarization, which is nonexistence in the present calculations. Furthermore, there is no evidence in experimental maps of any core polarizations (see Figure 2). Again, at least within the selected atomic properties, the characteristics of the Rh1 atom appear to be very similar in the nearly isostructural complexes **1c** and **1z** and, as such, would be expected to have a similar chemistry, perturbed to some extent by the differing electronic environments in the two related complexes.

The P1 Atom. This atom is consistently more positively charged in the theoretical model (by 0.138/0.116 au) in the zwitterionic complex **1z** than it is in the cationic relative **1c**. Of particular interest with regard to the conventional organometallic representations that are employed for such complexes is the observation that in both cationic **1c** and neutral **1z** the P atom, not the Rh atom, bears the greater net positive charge. This P atom is more compact in **1z** (with its volume being smaller by 4.8/4.8/2.7 au) and considerably less stable in **1c** (by 57.8 kcal mol^{-1}).

The N1 Atom. This atom is more negatively charged in the calculated densities (by 0.155/0.023 au) in the zwitterionic complex **1z** than it is in the cationic complex **1c**, in keeping with the electronegative nature of N and pointing to "leakage" of the electron density from the indenide unit in **1z**. This atom, however, bears an equally negative charge in the two complexes within experimental uncertainties. This atom is smaller in size in **1z** (by 1.0/0.5/0.4 au) but almost isoergic with respect to its counterpart in **1c** (less stable by 1.9 kcal mol^{-1}).

The Cn (n = 12, 13, 16, 17) Atoms. The C atoms bonded to Rh1 are all negatively charged [with $q(Cn) \approx -0.1$ to -0.4 au] without exhibiting striking trends in the atomic properties.

4.6. Comparison of the Group Properties in 1c and 1z. Figure 6 displays the net charge (q) and the volume (Vol) of five regions in **1c** (in au) obtained from the opt set of calculation. The changes in these properties, Δq and ΔVol, respectively, as well as the changes in the energies ΔE (in kcal mol^{-1}) for these five groups are given for **1z**.

The group properties and their changes upon the formal removal of the C1−H2 proton from **1c** to give **1z** are revealing (Figure 6). First, the total complex energy rises considerably by the removal of this proton, with the overall change in the energy of the reaction (i.e., **1c** → **1z** + H$^+$ = 273 kcal mol^{-1}) being primarily due to the loss of more electron−nuclear attractive (negative) energy than the reduction in the nuclear−nuclear repulsion. The loss of the H2 proton also causes the total electron density of the system to be slightly more diffuse; thus, the volume increases by ∼28 au in **1z** compared to **1c** (despite of having one less atomic basin in **1z**). In percentage terms, however, the change in the volume due to the removal of the proton is only ca. −0.8%. The energetic destabilization due to the deprotonation of **1c** overwhelms the necessarily stabilizing increase in the magnitude of exchange between the basins of the indenide fragment with its extended aromaticity in **1z** (two fused aromatic rings), relative to an isolated aromatic (benzene) ring in **1c**. Along with bond-length equalization, the indenide ring (particularly the 5-MR) becomes considerably more aromatic in **1z** compared to the indene unit in **1c** [the nucleus-independent chemical shifts (NICSs)[92,93] calculated at the centroids of the 6-MR and 5-MR for the two compounds are −13.7 and −1.8 ppm for **1c** and −14.8 and −21.7 ppm for **1z**, respectively (Table S.4 in the Supporting Information)].

Destabilization of **1z** with respect to **1c** is associated primarily with the indenide framework (+285 kcal mol^{-1}), but also from the Rh1 atom itself (+24 kcal mol^{-1}), compared to their counterparts in **1c**. In **1z** (compared to **1c**), the electronic charge is transferred from Rh1 to all of its neighboring groups. Thus, the R_P group gains 0.06 electrons, increases in volume by 3.3 au, and is destabilized by 16 kcal mol^{-1}; the R_N group gains 0.08 electrons, increases in volume

dx.doi.org/10.1021/ic2026347 | Inorg. Chem. 2012, 51, 3754−3769

by 1.9 au, and is stabilized by 22 kcal mol^{-1}; the COD group gains 0.14 electrons, increases in volume by 6.0 au, and is stabilized by 30 kcal mol^{-1}. Together, the three groups attached to Rh1 acquire 0.28 electrons, expand in size by 11.2 au, and are stabilized, as a result, by a total of approximately 36 kcal mol^{-1}. When the changes of all of the groups except those associated with the indene (**1c**)/indenide (**1z**) fragment are summed together, this subsystem gains a total of 0.27 electrons, increases in size by 19.6 au, and is stabilized by only 12.4 kcal mol^{-1}; when summed with ΔE(indenide/indene), the energy difference between the two complexes is obtained.

These observations indicate that the response of complex **1c** to the loss of proton H2 (thereby transforming the indene structure in **1c** into an indenide fragment in **1z**) results in a drastic electronic structure reorganization, primarily within the incipient indenide framework, leaving the essential features of Rh1 and its immediate surroundings relatively unchanged in **1z** relative to **1c**.

4.7. Topography of the Molecular Electrostatic Potential (ESP) (V(r)). The molecular ESP, $V(\mathbf{r})$, is defined as

$$V(\mathbf{r}) = \sum_{A} \frac{Z_A}{|\mathbf{R}_A - \mathbf{r}|} - \int \frac{\rho(\mathbf{r}')}{|\mathbf{r}' - \mathbf{r}|}\, d\mathbf{r}' \qquad (3)$$

where Z_A is the charge of nucleus A at the position R_A and $\rho(\mathbf{r}')$ is the electron density obtained from theoretical calculations or from multipolar modeling.[94]

The evidence presented in the previous sections suggests that the primary region of interest with regard to stoichiometric and catalytic reactivity involving **1c** and **1z**, namely, the Rh1 atom and its immediate surroundings, remains unaffected by the formal removal of the proton H2 in **1c** to afford **1z**. The most drastic changes in the bond, atomic, and group properties that accompany this deprotonation are relegated to the carbocyclic backbone of the ancillary P,N ligand. As can be seen from eq 3, the ESP is determined by the *total* charge density that results from two contributions: (a) The discrete distribution of the pointlike nuclear charge (first term) and (b) the continuous diffuse electronic charge (second term). The first term is completely determined by the geometry $\{\mathbf{R}_A\}$ (and the charges of the nuclei), while the second term is determined by the density $\rho(\mathbf{r})$. The similarity of both the geometry and electron density in the rhodium coordination sphere surrounding Rh1 in **1c** and **1z** is tantamount to the similarity of the corresponding region in their respective molecular ESP. On the other hand, the indene and indenide backbones of the ancillary P,N ligands in **1c** and **1z** (respectively) are expected to exhibit marked differences given that their geometries, electronic charges, and nuclear potentials are drastically different in the two complexes.

The anticipated similarity of the shape of the ESP in the two complexes, irrespective of the orientation, can be visually appreciated from Figure 7, which gives two side views of the calculated (sp) ESP for the two opposite faces of each of **1c** and **1z**. Furthermore, Figure 8 compares the experimentally determined ESP of the two complexes; in this case, the ESP of the **1c** complex is determined in the presence of its counteranion. Despite this significant perturbation, the displayed (representative) isosurfaces of the ESP around the Rh centers in **1c** and **1z** do no differ significantly.

Thus, the general topography of the ESP of **1z** around the Rh1 atom bears a striking similarity to that around the Rh1 atom of **1c**. Indeed, the differences that arise can be attributed entirely to the differing carbocyclic backbone frameworks in **1c**

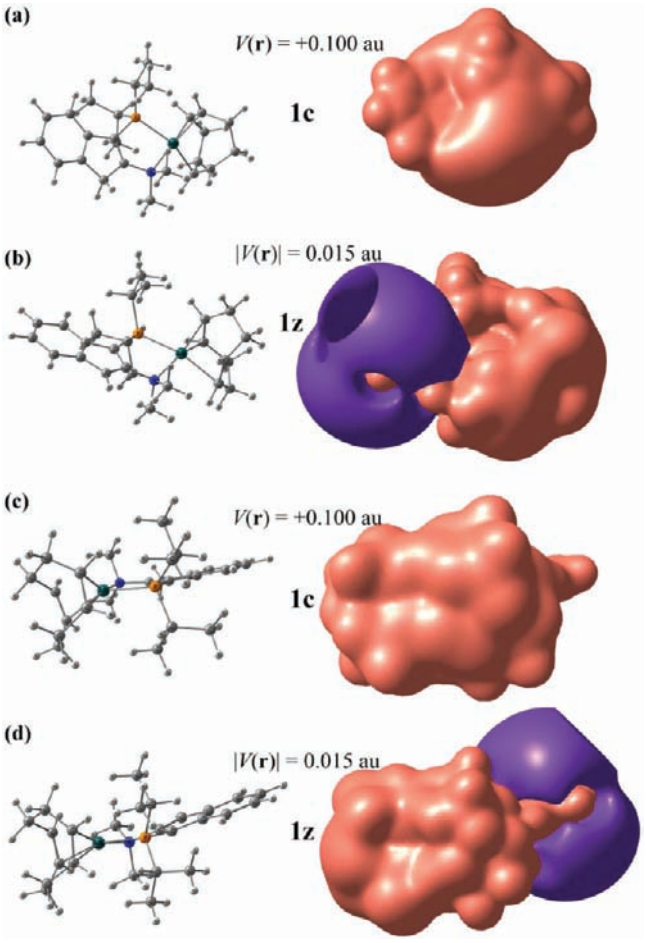

Figure 7. Calculated (sp) molecular ESP of the two complexes: Two isosurfaces (of magnitudes 0.100 and 0.015 au) showing that the similarity of the forms of the ESPs around the two faces of the catalytic center carries to more than one value of the ESP. On the left is a representation of the molecular geometry in the orientation used to generate the corresponding potential on the right. Color scheme: red, positive ESP; violet, negative ESP. (a and b) Orientations where the aromatic ring is on the left of the figure. (c and d) Rotated (roughly) by 180° to show the "back" of the molecule (the aromatic system is on the right of the figure).

and **1z**. The ESP in the **1z** complex exhibits a clear demarcation nodal surface (a surface whereby the ESP = 0) that splits the molecule into two parts: A quasi-intact Rh fragment and an

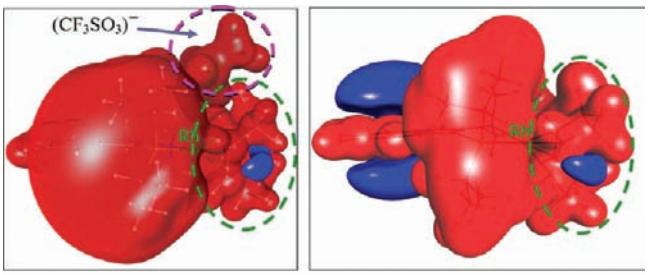

Figure 8. Experimentally determined molecular ESP at an isosurface with $|V(\mathbf{r})| = 0.05$ au that shows the similarity of the form of the ESP around the Rh atom (red, negative ESP; blue, positive ESP).

dx.doi.org/10.1021/ic2026347 | Inorg. Chem. 2012, 51, 3754–3769

indenide moiety that carries the burden of most of the changes (i.e., added negative charge) induced by the formal removal of a proton from C2 in **1c**. Figures 9 and 10 show a clear

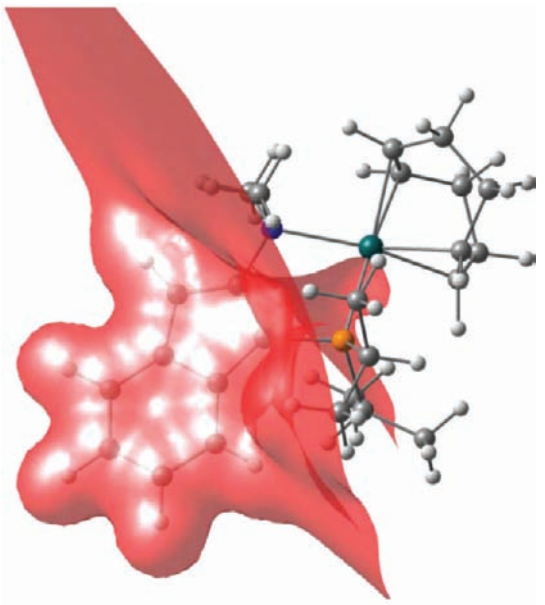

Figure 9. Calculated (sp) molecular ESP nodal surfaces [$V(\mathbf{r})$ = 0.000 au] of the **1z** complex. The nodal surface partitions the complex into a region of negative ESP from the side of the aromatic system and a region of positive ESP surrounding the catalytic center that has a topography similar to that of this region in **1c**.

demarcation between the two regions of **1z**, as can be seen from the shape of the nodal surface in $V(\mathbf{r})$.

Because it is the electric field $\mathbf{E}(\mathbf{r})$ that determines the trajectory of an approaching charged reactant and because $\mathbf{E}(\mathbf{r})$ is uniquely determined by the ESP [$\mathbf{E}(\mathbf{r}) = -\nabla V(\mathbf{r})$], the shape of the potential determines the direction of the approach and then demonstrates the similarity of the metal-centered reactivity of both complexes. The consistency of the results obtained at two different levels of theory (level 1 and 2), Figures 9 and 10, with one set of calculations (level 2) even conducted on truncated models of **1c** and **1z** (namely **1c′** and **1z′**, Chart 1) indicate that these results are insensitive to either the level of theory or the molecular model used to represent the cationic and zwitterionic complexes.

5. CONCLUDING REMARKS

Highly accurate electron-density distributions of structurally analogous cationic (**1c**) and zwitterionic (**1z**) organometallic complexes were determined from accurate synchrotron X-ray diffraction experiments and a high level of computational theory. The strong agreement found between the experimental and theoretical results provides considerable support to the conclusions summarized herein.

A comparison of the geometries, electron distributions, electron delocalization, and molecular ESPs in these two complexes reveals a striking feature: The two complexes are very similar within the Rh1 coordination sphere and differ (quite significantly) only with regard to the properties associated with the indene (**1c**) and indenide (**1z**) frameworks. These similarities *and* differences are equally important with regard to confirming the postulate that appropriately designed

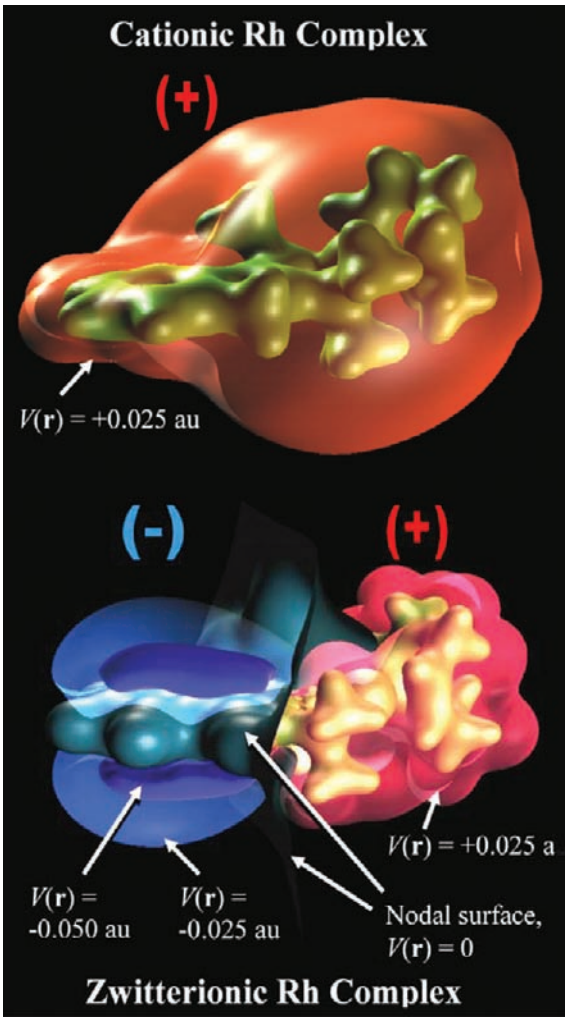

Figure 10. Calculated molecular ESP, $V(\mathbf{r})$, in transparent envelopes, for truncated models of **1c′** (top) and **1z′** (bottom) (the *tert*-butyl groups attached to the P atom are replaced by methyl groups, see Chart 1). (The calculations were conducted at the level of theory called "level 2", described in Section 4.5 of the text). The red and blue envelopes represent positive and negative potentials, respectively, while the darker surface (in **1z′**) that surrounds the aromatic ring and splits the molecule into the aromatic side (left) and rhodium side (right) is the nodal surface separating the regions of positive and negative ESP. The inner solid golden surface isosurface of $\rho(\mathbf{r})$ = 0.1 au is a high-electron-density envelope in the region close to the nuclear framework of the complexes. The ESP of **1c′** (top) is clearly positive everywhere (up to the chosen isosurface) with a depression near the aromatic ring. The ESP of **1z′**, however, zwitterionic is partitioned by the nodal surface into two contiguous regions of positive and negative values, with the latter region exhibiting increasingly more negative values the closer the isosurface is to the aromatic ring [the inner dark envelope of $V(\mathbf{r}) = -0.05$ au].

zwitterionic platinum-group metal complexes (such as **1z**) can serve as charge-neutral variants of more conventional cationic species (such as **1c**) in reactivity applications. Indeed, in keeping with the results of our catalytic experiments,[18] **1z** is predicted to exhibit metal-centered reactivity behavior that is reminiscent of **1c** due to the minimal steric and electronic perturbation that are observed in the metal coordination sphere on going from **1c** to **1z**. Furthermore, the reasonably efficient sequestration of charge on the conjugated carbocyclic P,N-ligand backbone in **1z** enforces *considerable zwitterionic*

dx.doi.org/10.1021/ic2026347 | *Inorg. Chem.* 2012, 51, 3754–3769

character in this species [the indenide fragment carries charges (in au) of −0.754 (experiment) and −0.924 and −0.918 (theory: single point at the experimental geometry and after geometry optimization, respectively), and the rest of the molecule carries an equal and oppositely distributed positive charge]. We envision that having confirmed herein that donor-substituted indenide ligands can support genuinely zwitterionic (charge-separated) platinum-group metal organometallic complexes that exhibit properties reminiscent of their cationic counterparts will encourage the further development and study of this and other classes of zwitterionic platinum-group metal complexes.

■ ASSOCIATED CONTENT

Supporting Information

X-ray crystallographic CIF files of the two complexes **1c** and **1z**, four *Gaussian09* extended wave function files of the two complexes, calculated at the experimental and optimized geometries, augmented with rhodium core densities (these text files can also be read by *AIMAll/AIMStudio*), a table of selected experimental and optimized bond lengths and angles (Table S.1), tables of experimental and optimized Cartesian coordinates (Tables S.2 and S.3 for **1c** and **1z**, respectively), a table listing the correspondence of the experiment atomic numbering/labeling schemes to the serial atomic numbering as in the theoretical wave function files calculated from *Gaussian09* (Table S.4), a listing of the calculated NICSs at the three ring centers of **1c** and **1z** (Table S.5), residual density maps (Figure S1), a representation of the molecular graphs of the two complexes (Figure S2), and finally comparative plots of the Laplacian of the electron density in three planes containing the rhodium metal from the three data sets for the two complexes (Figure S3). This material is available free of charge via the Internet at http://pubs.acs.org.

■ AUTHOR INFORMATION

Corresponding Author

*E-mail: cherif.matta@msvu.ca (C.F.M.), claude.lecomte@crm2.uhp-nancy.fr(C.L.).

Notes

The authors declare no competing financial interest.

■ ACKNOWLEDGMENTS

The authors are very grateful to Dr. Kevin Hesp (Stradiotto Group, Dalhousie University) for growing the single crystals that were used in this study. E.-E.B. is grateful to Professors Sylvain Ravy and Erik Elkaïm of CRISTAL beamline at Synchrotron Soleil for many helpful discussions and to Drs. Benoit Guillot and Bertrand Fournier for *VMoPro* and *MoProViewer* tutorials. Professor Kirk A. Peterson (Washington State University) is thankfully acknowledged for his useful insight about the use of tight functions on P atoms. We are also very grateful to Fabien Legrand (Synchrotron Soleil) for technical assistance. C.F.M. acknowledges financial support of the Natural Sciences and Engineering Research Council of Canada (NSERC), Canada Foundation for Innovation (CFI), and Mount Saint Vincent University. C.F.M. is also grateful for several Visiting Professorships at the Université Henri Poincaré (now Université de Lorraine) in 2007−2011, during which time most of this work had been completed. M.S. thanks NSERC, the Killam Trusts, and Dalhousie University for their generous support of this work.

■ DEDICATION

†This paper is dedicated to the memory of Professor Richard F. W. Bader (who passed away on Jan 15, 2012, at the age of 80), the pioneer who developed the quantum theory of atoms in molecules and the topological analysis of molecular scalar and vector fields.

■ REFERENCES

(1) Knowles, W. S. *Angew. Chem., Int. Ed.* **2002**, *41*, 1998−2007.
(2) Bell, S.; Wüstenberg, B.; Kaiser, S.; Menges, F.; Netscher, T.; Pfaltz, A. *Science* **2006**, *311*, 642−644.
(3) Schrock, R. R.; Osborn, J. A. *J. Am. Chem. Soc.* **1976**, *98*, 2134−2143.
(4) Schrock, R. R.; Osborn, J. A. *J. Am. Chem. Soc.* **1976**, *98*, 2143−2147.
(5) Crabtree, R. *Acc. Chem. Res.* **1979**, *12*, 331−337.
(6) Källström, K.; Munslow, I.; Andersson, P. G. *Chem.—Eur. J.* **2006**, *12*, 3194−3200.
(7) Macchioni, A. *Chem. Rev.* **2005**, *105*, 2039−2074.
(8) Smidt, S. P.; Zimmermann, N.; Studer, M.; Pfaltz, A. *Chem.—Eur. J.* **2004**, *10*, 4685−4693.
(9) Stradiotto, M.; Hesp, K. D.; Lundgren, R. J. *Angew. Chem., Int. Ed.* **2010**, *49*, 494−512.
(10) Amer, I.; Alper, H. *J. Am. Chem. Soc.* **1990**, *112*, 3674−3676.
(11) Betley, T. A.; Peters, J. C. *Angew. Chem., Int. Ed.* **2003**, *42*, 2385−2389.
(12) Lundgren, R. J.; Rankin, M. A.; McDonald, R.; Schatte, G.; Stradiotto, M. *Angew. Chem., Int. Ed.* **2007**, *46*, 4732−4735.
(13) Coppens, P. *X-ray Charge Densities and Chemical Bonding*; Oxford University Press, Inc.: New York, 1997.
(14) Lecomte, C.; Aubert, E.; Legrand, V.; Porcher, F.; Pillet, S.; Guillot, B.; Jelsch, C. *Z. Kristallogr.* **2005**, 373−384.
(15) Bader, R. F. W. *Atoms in Molecules: A Quantum Theory*; Oxford University Press: Oxford, U.K., 1990.
(16) Popelier, P. L. A. *Atoms in Molecules: An Introduction*; Prentice Hall: London, 2000.
(17) Matta, C. F.; Boyd, R. J. *The Quantum Theory of Atoms in Molecules: From Solid State to DNA and Drug Design*; Wiley-VCH: Weinheim, Germany, 2007.
(18) Stradiotto, M.; Cipot, J.; McDonald, R. *J. Am. Chem. Soc.* **2003**, *125*, 5618−5619.
(19) Cipot, J.; McDonald, R.; Ferguson, M. J.; Schatte, G.; Stradiotto, M. *Organometallics* **2007**, *26*, 594−608.
(20) Santi, S.; Ceccon, A.; Crociani, L.; Gambaro, A.; Ganis, P.; Tiso, M.; Venzo, A.; Bacchi, A. *Organometallics* **2002**, *21*, 565−574.
(21) Schumann, H.; Stenzel, O.; Dechert, S.; Girgsdies, F.; Blum, J.; Gelman, D.; Halterman, R. L. *Eur. J. Inorg. Chem.* **2002**, 211−219.
(22) Rupert, K. C.; Liu, C. C.; Nguyen, T. T.; Whitener, M. A.; Sowa, J. R. Jr. *Organometallics* **2002**, *21*, 144−149.
(23) Schumann, H.; Stenzel, O.; Dechert, S.; Girgsdies, F.; Halterman, R. L. *Organometallics* **2001**, *20*, 5360−5368.
(24) Schumann, H.; Stenzel, O.; Dechert, S.; Girgsdies, F.; Halterman, R. L. *Organometallics* **2001**, *20*, 2215−2225.
(25) Westcott, S. A.; Kakkar, A. K.; Taylor, N. J.; Roe, D. C.; Marder, T. B. *Can. J. Chem.* **1999**, *77*, 205−215.
(26) CrysAlisCCD. *CrysAlisRED*, version 1.171.33.13; Oxford Diffraction Ltd.: Abingdon, Oxfordshire, England, 2008.
(27) Blessing, R. H. *J. Appl. Crystallogr.* **1997**, *30*, 421−426.
(28) Sheldrick, G. M. *SHELXS97 and SHELXL97: programs for crystal structure refinement*; University of Gottingen: Gottingen, Germany, 1997.
(29) Sheldrick, G. M. *Acta Crystallogr., Sect. A* **2008**, *64*, 112−122.
(30) Farrugia, L. J. *WinGX*, version 1.64.05; 1999.
(31) Farrugia, L. J. *J. Appl. Crystallogr.* **1999**, *32*, 837−838.
(32) Hansen, N. K.; Coppens, P. *Acta Crystallogr.* **1978**, *A34*, 909−921.
(33) Guillot, B.; Viry, L.; Guillot, R.; Lecomte, C.; Jelsch, C. J. *J. Appl. Crystallogr.* **2001**, *34*, 214−223.

(34) Jelsch, C.; Guillot, B.; Lagoutte, L.; Lecomte, C. MoProViewer: a Molecular Viewer Dedicated to Charge Density Analysis. Poster, French Crystallographic Assocociation AFC2010, Strasbourg, France, July 7−10, 2010, http://www.crm2.uhp-nancy.fr/crm2/ fr/labo/equipes/emqc/.
(35) Su, Z.; Coppens, P. *Acta Crystallogr., Sect. A* **1998**, *54*, 646−652.
(36) Macchi, P.; Coppens, P. *Acta Crystallogr., Sect. A* **2001**, *57*, 656−662.
(37) Stewart, R. F.; Davidson, E. R.; Simpson, W. T. *J. Chem. Phys.* **1965**, *42*, 3175−3187.
(38) Volkov, A.; Abramov, Y.; Coppens, P. *Acta Crystallogr., Sect. A* **2001**, *57*, 272−282.
(39) Allen, F. H.; Kennard, O.; Watson, D.; Brammer, L.; Orpen, A.; Taylor, R. *International Tables for Crystallography*; Kluwer Academic Publishers: Dordrecht, The Netherlands, 1992; Vol. *C*, Chapter 9.5, pp 685−706.
(40) Madsen, A. Ų. *J. Appl. Crystallogr.* **2006**, *39*, 757−758.
(41) Hirshfeld, F. L. *Acta Crystallogr., Sect. A* **1976**, *32*, 239−244.
(42) Macchi, P.; Proserpio, D. M.; Sironi, A. *J. Am. Chem. Soc.* **1998**, *120*, 1447−1455.
(43) Stash, A.; Tsirelson, V. *J. Appl. Crystallogr.* **2002**, *35*, 371−373.
(44) Parr, R. G.; Yang, W. *Density Functional Theory of Atoms and Molecules*; Oxford University Press: Oxford. U.K., 1989.
(45) Koch, W.; Holthausen, M. C. *A Chemist's Guide to Density Functional Theory*, 2nd ed.; Wiley-VCH: New York, 2001.
(46) Lee, C.; Yang, W.; Parr, R. *Phys. Rev. B* **1988**, *37*, 785−789.
(47) Becke, A. *J. Chem. Phys.* **1993**, *98*, 5648−5652.
(48) Chesnut, D. B.; Rusiloski, B. E.; Moore, K. D.; Egolf, D. A. *J. Comput. Chem.* **1993**, *14*, 1364−1375.
(49) Chesnut, D. B.; Byrd, E. F. C. *J. Comput. Chem.* **1996**, *17*, 1431−1443.
(50) DiLabio, G. A.; Wright, J. S. *Chem. Phys. Lett.* **1998**, *297*, 181−186.
(51) DiLabio, G. A. *J. Phys. Chem. A* **1999**, *103*, 11414−11424.
(52) Cramer, C. J. *Essentials of Computational Chemistry: Theories and Models*; John Wiley & Sons, Ltd.: New York, 2002.
(53) Jensen, F. *Introduction to Computational Chemistry*; John Wiley and Sons Ltd.: West Sussex, U.K., 2007.
(54) Peterson, K. A. F. D.; Dolg, M.; Stoll, H. *J. Chem. Phys.* **2007**, *126*, 124101_1−124101_12.
(55) Prascher, B.; Woon, D.; Peterson, K.; Dunning, T.; Wilson, A. *Theor. Chim. Acta* **2011**, *128*, 69−82.
(56) Tiana, D.; Francisco, E.; Blanco, M. A.; Martin Pendas, A. *J. Phys. Chem. A* **2009**, *113*, 7963−7971.
(57) Keith, T. A.; Frisch, M. J. *J. Phys. Chem. A* **2011**, *115*, 12879−12894.
(58) de Castro, E. V. R.; Jorge, F. E. *J. Chem. Phys.* **1998**, *108*, 5225−5229.
(59) Douglas, M.; Kroll, N. M. *Ann. Phys. (N.Y.)* **1974**, *82*, 89−155.
(60) Hess, B. A. *Phys. Rev. A* **1985**, *32*, 756−763.
(61) Hess, B. A. *Phys. Rev. A* **1986**, *33*, 3742−3748.
(62) Jansen, G.; Hess, B. A. *Phys. Rev. A* **1989**, *39*, 6016−6017.
(63) Frisch, M. J.; Trucks, G. W.; Schlegel, H. B.; Scuseria, G. E.; Robb, M. A.; Cheeseman, J. R.; Scalmani, G.; Barone, V.; Mennucci, B.; Petersson, G. A.; Nakatsuji, H.; Caricato, M.; Li, X.; Hratchian, H. P.; Izmaylov, A. F.; Bloino, J.; Zheng, G.; Sonnenberg, J. L.; Hada, M.; Ehara, M.; Toyota, K.; Fukuda, R.; Hasegawa, J.; Ishida, M.; Nakajima, T.; Honda, Y.; Kitao, O.; Nakai, H.; Vreven, T.; Montgomery, J. A., Jr.; Peralta, J. E.; Ogliaro, F.; Bearpark, M.; Heyd, J. J.; Brothers, E.; Kudin, K. N.; Staroverov, V. N.; Keith, T.; Kobayashi, R.; Normand, J.; Raghavachari, K.; Rendell, A.; Burant, J. C.; Iyengar, S. S.; Tomasi, J.; Cossi, M.; Rega, N.; Millam, J. M.; Klene, M.; Knox, J. E.; Cross, J. B.; Bakken, V.; Adamo, C.; Jaramillo, J.; Gomperts, R.; Stratmann, R. E.; Yazyev, O.; Austin, A. J.; Cammi, R.; Pomelli, C.; Ochterski, J. W.; Martin, R. L.; Morokuma, K.; Zakrzewski, V. G.; Voth, G. A.; Salvador, P.; Dannenberg, J. J.; Dapprich, S.; Daniels, A. D.; Farkas, O.; Foresman, J. B.; Ortiz, J. V.; Cioslowski, J.; Fox, D. J. *Gaussian 09*, revision B.01; Gaussian Inc.: Wallingford, CT, 2010.
(64) Keith, T. A. *AIMAll*, version 11.05.16, Professional; 2011, aim@tkgristmill.com.
(65) Dunning, T. H.; Peterson, K. A.; Wilson, A. K. *J. Chem. Phys.* **2001**, *114*, 9244−9253.
(66) *EMSL Basis Set Exchange*; EMSL Office of Science: Washington, DC, 2011, https://bse.pnl.gov/bse/portal.
(67) Peterson, K. A. *Personal communication*, 2011.
(68) Sparkes, H. A.; Brayshaw, S. K.; Weller, A. S.; Howard, J. A. K. *Acta Crystallogr., Sect. B* **2008**, *64*, 550−557.
(69) Runtz, G. R.; Bader, R. F. W.; Messer, R. R. *Can. J. Chem.* **1977**, *55*, 3040−3045.
(70) Bader, R. F. W. *J. Phys. Chem. A* **1998**, *102*, 7314−7323.
(71) Bader, R. F. W. *J. Phys. Chem. A* **2009**, *113*, 10391−10396.
(72) Fradera, X.; Austen, M. A.; Bader, R. F. W. *J. Phys. Chem. A* **1999**, *103*, 304−314.
(73) Martin Pendas, A.; Francisco, E.; Blanco, M. A.; Gatti, C. *Chem.—Eur. J.* **2007**, *13*, 9362−9371.
(74) Bader, R. F. W.; Matta, C. F. *Inorg. Chem.* **2001**, *40*, 5603−5611.
(75) Matta, C. F.; Hernández-Trujillo, J. *J. Phys. Chem. A* **2003**, *107*, 7496−7504 (Correction: *J. Phys. Chem A* **2005**, *109*, 10798).
(76) Macchi, P.; Sironi, A. *Coord. Chem. Rev.* **2003**, *238−239*, 383−412.
(77) Matta, C. F.; Hernández-Trujillo, J.; Tang, T. H.; Bader, R. F. W. *Chem.—Eur. J.* **2003**, *9*, 1940−1951.
(78) Paul, A.; Kubicki, M.; Jelsch, C.; Durand, P.; Lecomte, C. *Acta Crystallogr., Sect. B* **2011**, *67*, 365−378.
(79) Hernández-Trujillo, J.; Matta, C. F. *Struct. Chem.* **2007**, *18*, 849−857.
(80) Matta, C. F. Hydrogen-hydrogen bonding: The non-electrostatic limit of closed-shell interaction between two hydrogen atoms. A critical review. In *Hydrogen Bonding—New Insight (Challenges and Advances in Computational Chemistry and Physics Series)*; Grabowski, S., Ed.; Springer: Berlin, 2006; pp 337−376.
(81) Bakhmutov, V. I. *Dihydrogen Bonds: Principles, Experiments, and Applications*; Wiley-Interscience: New York, 2008.
(82) Farrugia, L. J.; Evans, C.; Lentz, D.; Roemer, M. *J. Am. Chem. Soc.* **2009**, *131*, 1251−1268.
(83) Sparkes, H. A.; Chaplin, A. B.; Weller, A. S.; Howard, J. A. K. *Acta Crystallogr., Sect. B* **2010**, *66*, 503−514.
(84) Cremer, D.; Kraka, E. *Angew. Chem., Int. Ed. Engl.* **1984**, *23*, 627−628.
(85) Rohrmoser, B.; Eickerling, G.; Presnitz, M.; Scherer, W.; Eyert, V.; Hoffmann, R.-D.; Rodewald, U. C.; Vogt, C.; Pųttgen, R. J. *J. Am. Chem. Soc.* **2007**, *129*, 9356−9365.
(86) Dewar, M. J. S. *Bull. Soc. Chim. Fr.* **1951**, *18*, C71−C79.
(87) Chatt, J.; Duncanson, L. A. *J. Chem. Soc.* **1953**, 2939−2947.
(88) Macchi, P.; Sironi, A. Metal involving interactions: From "chemical categories" to QTAIM and backwards. In *The Quantum Theory of Atoms in Molecules: From Solid State to DNA and Drug Design*; Matta, C. F., Boyd, R. J., Eds.; Wiley-VCH: Weinheim, Germany, 2007.
(89) Scherer, W.; Eickerling, G.; Shorokhov, D.; Gullo, E.; McGrady, G. S.; Sirsch, P. *New J. Chem.* **2006**, *30*, 309−312.
(90) Nuss, H.; Claiser, N.; Pillet, S.; Lugan, N.; Despagnet-Ayoub, E.; Etienne, M.; Lecomte, C. *Dalton Trans.* **2012**, submitted.
(91) Coppens, P.; Iversen, B.; Larsen, F. K. *Coord. Chem. Rev.* **2005**, *249*, 179−195.
(92) Chen, Z.; Wannere, C. S.; Corminboeuf, C.; Puchta, R.; Schleyer, P. v. R. *Chem. Rev.* **2005**, *105*, 3842−3888.
(93) Schleyer, P.v-R.; Maerker, C.; Dransfeld, A.; Jiao, H.; Hommes, N. J. R. v. E. *J. Am. Chem. Soc.* **1996**, *118*, 6317−6318.
(94) Ghermani, N.; Bouhmaida, N.; Lecomte, C. *ELECTROS: A Computer Program to Calculate Electrostatic Properties from High Resolution X-ray Diffraction*; Internal Report URA CNRS 809; University of Nancy 1: Nancy, France, 1992.
(95) Macrae, C. F.; Bruno, I. J.; Chisholm, J. A.; Edgington, P. R.; McCabe, P.; Pidcock, E.; Rodriguez-Monge, L.; Taylor, R.; van de Streek, J.; Wood, P. A. *J. Appl. Crystallogr.* **2008**, *41*, 466−470.